Journal of the European Ceramic Society 45 (2025) 117348

Contents lists available at ScienceDirect

Journal of the European Ceramic Society

journal homepage: www.elsevier.com/locate/jeurceramsoc

Original article

Design of a functional steam electrode for Proton-conducting ceramic electrolysis cells based on $BaCo_{0.4}Fe_{0.4}Zr_{0.2}O_{3-\delta}$: $BaZr_{0.7}Ce_{0.2}Y_{0.1}O_{3-\delta}$ composite

Shivam Kumar Dwivedi [a,b,*], Laura-Alena Schaefer [c,b], Yuan Zeng [b,c], Yoo Jung Sohn [b], Jürgen Malzbender [d], Andreas Beyer [e], Celina Becker [e], Kerstin Volz [e], Norbert H. Menzler [c,b], Olivier Guillon [c,b,f], Mariya E. Ivanova [b,**], Ravi Kumar [a,f,**]

[a] Laboratory for High Performance Ceramics, Department of Metallurgical and Materials Engineering, Indian Institute of Technology-Madras (IIT Madras), Chennai, 600036, India
[b] Institute of Energy Materials and Devices – Materials Synthesis and Processing (IMD-2), Forschungszentrum Jülich GmbH, Jülich, 52428, Germany
[c] Department of Ceramics and Refractory Materials, Institute of Mineral Engineering, RWTH Aachen University, Aachen, 52078, Germany
[d] Institute of Energy Materials and Devices – Microstructure and Properties of Materials (IMD-1), Forschungszentrum Jülich GmbH, Jülich, 52428, Germany
[e] Materials Science Center and Faculty of Physics, Philipps-University Marburg, Hans-Meerweinstraße 6, Marburg, 35032, Germany
[f] Research Center on Ceramic Technologies for Futuristic Mobility, Institute of Eminence (IoE), Indian Institute of Technology-Madras (IIT Madras), Chennai, 600036, India

ARTICLE INFO

Keywords:
Proton-conducting ceramic electrolysis cells (PCECs)
Steam electrode
Mixed proton-electronic conducting ceramic materials
Functional layer
BCFZ
BZCY

ABSTRACT

A key issue in the steam electrode development for Proton-conducting Ceramic Electrolysis Cells (PCECs) is the required contact with the electrolyte material as well as thermo-chemical compatibility during cell processing and operation. This study focuses on $BaCo_{0.4}Fe_{0.4}Zr_{0.2}O_{3-\delta}$ (BCFZ442) as a potential steam electrode material paired with the state-of-the-art proton conductor $BaZr_{0.7}Ce_{0.2}Y_{0.1}O_{3-\delta}$ (BZCY721). The objectives are to identify an optimal material composition amongst several compositional variations and to define its corresponding fabrication conditions for achieving suitable electrodes compatibility, adhesion and performance for further translation into the cell fabrication process. Therefore, we tested 90:10, 70:30 and 50:50 BCFZ442:BZCY721 composites which were heat-treated in the temperature of 800–1200 °C. The phase evolution accompanied by thermal and microstructural analyses and in addition to electrical and mechanical characterization yielded interesting results. Extensive analysis indicate compositional, functional and fabrication optimum in the steam electrode development of PCECs.

1. Introduction

The world's population, economy, and urbanization are expanding rapidly, increasing the energy demand. At the same time, the contribution of renewable energy is also growing and expected to rise globally from 30% in 2023 to 37% in 2026, with the growth largely supported by the expansion of solar and wind [1]. However, solar and wind energy is location- and weather-dependent, which creates intermittency in the energy supply. Thus, reliable and affordable large-scale electricity storage methods are needed [2,3]. Converting electricity to fuels/chemicals, specifically H_2 by electrolysis is an elegant way to store large-scale electricity compared to battery-based storage systems [3,4]. Among the different types of electrolysis technologies, Solid Oxide Cell (SOC) steam electrolysis offers the highest energy efficiencies for H_2 production, i.e., ≥ 95% if operated thermoneutrally [5]. Additionally, SOECs are considered capable of electrolysis of CO_2 and co-electrolysis of CO_2 and H_2O, which is a promising approach to the production of syngas or further chemicals, and generally for CO_2 utilization [3,6,7].

Amongst the high-temperature SOECs technology, a new class of electrolyzers based on proton-conducting ceramic materials has attracted much attention in recent years. Proton ceramic electrolysis cells (PCECs) indeed possess some unique merits over oxygen-conducting electrolysis cells, such as the purity of H_2 produced without the necessity of an additional $H_2/H_2O + O_2$ separation step to be introduced

* Corresponding author at: Laboratory for High Performance Ceramics, Department of Metallurgical and Materials Engineering, Indian Institute of Technology-Madras (IIT Madras), Chennai, 600036, India.
** Corresponding authors.
E-mail addresses: dwivedis@alumni.iitm.ac.in (S.K. Dwivedi), m.ivanova@fz-juelich.de (M.E. Ivanova), nvrk@iitm.ac.in (R. Kumar).

https://doi.org/10.1016/j.jeurceramsoc.2025.117348
Received 18 October 2024; Received in revised form 24 February 2025; Accepted 3 March 2025
Available online 14 March 2025

to the system periphery, as well as moderately elevated operating temperature (400–600 °C) resulting from the thermodynamic nature of the mobile charge carriers (protons) in PCECs.

PCECs are typically based on the B-site substituted $BaZrO_3$-$BaCeO_3$ (BZC) solid solutions as electrolyte, BZC:Ni-based cermets [8,9] as H_2 electrode, and Co-, Fe-, Mn-, Pr-rich perovskites serving as steam electrode [10–12]. Research and development activities are usually aimed at overcoming issues related to the cell performance, durability [10,13] and scalability. These materials- and cell-related aspects will be briefly considered in the next few paragraphs as they play an essential role in the conceptualization of the present work.

Solid electrolyte: $BaZr_{0.7}Ce_{0.2}Y_{0.1}O_{3-\delta}$ (BZCY721) is a state-of-the-art proton conductor, commonly used as solid electrolyte in the PCC cell design, which composition is the trade-off between the thermochemical stability, acceptor dopant solubility at elevated temperatures and the overall performance of the Y-substituted $BaZrO_3$ and $BaCeO_3$ classes of materials. By introduction of Y_2O_3 to the composition, Y^{3+} is substituted for the tetravalent Zr and Ce in the pristine lattice thus facilitating the formation of oxygen vacancies being necessary for the proton uptake of the material [14–18]. There are a number of review papers that exist in the literature that outline the multifaceted compositional variation based on Zr/Ce ratio for various applications [9,13,19–23].

Steam electrode: Over the past decade, various studies have been performed on definition and testing of new air/steam electrode materials for PCC fuel/electrolysis cells. Some examples include simple perovskite-type oxides such as $Sm_{0.5}Sr_{0.5}CoO_{3-\delta}$ (SSC) [24], $La_{1-x}Sr_xCo_{1-y}Fe_yO_{3-\delta}$ (LSCF) [25,26], $Ba_{0.5}Sr_{0.5}Co_{0.8}Fe_{0.2}O_{3-\delta}$ (BSCF) [25], $PrBa_{0.5}Sr_{0.5}Co_{2-x}Fe_xO_{5+\delta}$ [27], $SmBa_{0.5}Sr_{0.5}Co_2O_{5+\delta}$ [28], $La_{n+1}Ni_nO_{3n+1}$ (n = 1, 2, 3) [29], $GdBaCo_2O_{5+\delta}$ [30], $Ln_{0.4}Sr_{0.6}Co_{0.8}Fe_{0.2}O_{3-\delta}$ (Ln = La, Pr, Nd, Sm and Gd) [31], $BaCe_{0.4}Pr_{0.4}Y_{0.2}O_{3-\delta}$ [32], $La_{0.7}Sr_{0.3}FeO_{3-\delta}$ [33], and $Ba_{0.5}Sr_{0.5}Zn_{0.2}Fe_{0.8}O_{3-\delta}$ [34], $Sm_{0.5}Sr_{0.5}Fe_{0.8}Cu_{0.2}O_{3-\delta}$ [35]. Furthermore, the mentioned materials are not suitable for air electrodes with state-of-the-art proton conductors due to thermal expansion mismatch, instability in CO_2 and H_2O atmospheres, inconsistent electrochemical performance, and high material cost [36], restricting the scalability of PCECs. For example, $La_{0.60}Sr_{0.40}Co_{0.20}Fe_{0.80}O_{3-\delta}$ (LSCF), a widely studied SOFC air electrode material, has been investigated for PCEC air electrode [37,38]. However, reports indicate significant degradation for LSCF exposed to O_2–CO_2 (2.83%)–H_2O (2.64%) at 600 °C. This degradation is attributed to the formation of $SrCO_3$ on the surface, hindering oxygen activation and surface diffusion [3,39]. Similarly, $Ba_{0.50}Sr_{0.50}Co_{0.80}Fe_{0.20}O_{3-\delta}$ (BSCF) decomposes upon exposure to 75% H_2O–air at 426 K, rendering it unsuitable for H-SOEC air electrodes [26]. A crucial distinction here is that these materials were originally developed for oxygen-ion conducting cells [40–42] and directly applied in H-SOECs without considering the distinct interfacial reactions occurring with proton-conducting electrolytes.

Steam electrode reaction mechanism [43] in PCECs is distinct from that observed in SOECs/SOFCs, where oxygen ions have to also diffuse to the TPB area (TPB: triple-phase boundary defined as the critical junctions where the electronic conductor, the ionic conductor, and the gas phase converge). The air electrode materials used for SOECs/SOFCs cannot be directly used for PCECs because these materials only show good electronic and oxygen-ion conductivities with no protonic pathway, which is necessary for the whole air electrode reaction of PCECs. Furthermore, reaction sites are only restricted to the interface between the air electrode materials and the electrolyte layer, as shown in the graphical abstract figure. To extend the reaction sites, a rational approach is to make a composite air electrode material by mixing a proton conductor with an electronic or electronic/oxygen-ion mixed conductor [43]. Composite air electrode materials that incorporate a proton conductor with an electronic conductor (such as $BaCe_{0.5}Bi_{0.5}O_{3-\delta}\delta$ [44] $BaCe_{0.9}Yb_{0.1}O_{3-\delta}\delta$ [45] and $BaCe_{0.8-x}Pr_xO_{3-\delta}\delta$ [46]) offer a strategy to boost the reaction through extending the reaction sites. However, the poor chemical stability of $BaCeO_3$-based materials in the water-rich environments of PCECs poses a challenge. Consequently, compositions containing essential Zr content are being considered as more stable material candidates.

Limitation in the PCEC cell performance caused by the steam electrode–electrolyte interface: Issues in steam electrode development are related not only to the material selection, often including use of high costly elements, but also to the reduced performance due to, amongst others, polarization resistance, usually caused by not optimal contact to the electrolyte layer in the cell configuration.

To overcome contact resistance limitation of the PCEC, we will focus in the present work on designing steam electrode formulations with improved performance and compatibility to the BZCY721 electrolyte. For this purpose, Co and Fe rich $BaZrO_3$ (BCFZ442) was selected as steam electrode material. $BaCo_{0.4}Fe_{0.4}Zr_{0.2}O_{3-\delta}$ (BCFZ442) exhibits promising characteristics for long-term applications due to its mixed ionic–electronic conductivity, stable perovskite structure with large Ba^{2+} cations (facilitating oxygen ion migration), and good catalytic activity from Co/Fe valence state changes [47–52]. For instance, compared to $La_{0.6}Sr_{0.4}Fe_{0.8}Co_{0.2}O_{3-\delta}$ (LSCF), BCFZ442 demonstrates significantly lower polarization resistance (e.g., 8.5 vs. 65 Ω cm^2 at 500 °C, 1.6 vs 5.1 Ω cm^2 at 600 °C), further decreasing in humid air (3.9 and 1.0 Ω cm^2 at 500 and 600 °C, respectively) [53]. Furthermore, recent review papers [12,53] also pointed out the promising properties of steam electrodes based on BCFZ442 and Y-doped BCFZ442, amongst the electrodes mentioned above.

To address the cell performance limitations caused by poor interface contact with the electrolyte, a common approach involves a composite material [26,46,53,54] introduced as an intermediate electrode layer, hereafter referred to as the functional layer (FL), positioned between the electrolyte and the air electrode. The present study aims to identify the optimal material composition and the corresponding fabrication conditions such as paste formulation, sintering temperature etc., for achieving optimal microstructures, compatibility and adhesion, for further translation to the cell fabrication process.

2. Experimental procedure

2.1. Powders and characterization

We procured BZCY721 powder used as electrolyte (EL) from Marion Technologies, France, and BCFZ442 used in the development of steam electrode functional layer (FL) from CerPoTech, Norway. The powders were routinely characterized and their "as received" essential characteristics are summarized in Table 1. The chemical composition of the two powders was verified using Inductively coupled plasma – optical emission spectrometry (ICP-OES) (Thermo Fisher Scientific iCAP 7600 series). The phase composition and the crystal structure were analyzed via X-ray diffraction (XRD), (Bruker D4 Endeavor, USA) with CuK_α radiation. The particle size distribution and the specific surface area determined according to the BET method [55] were measured using Horiba LA-950b V2 and Micromeritics Tristar II, with nitrogen as the measurement gas at −196 °C, respectively.

2.2. Preparation of ceramic composites specimens

For the preparation of the ceramic composites, the initially delivered BZCY721(EL) powder was mixed with additionally ball-milled BCFZ442(FL) in various weight fractions, i.e., 90:10, 70:30 and 50:50 wt%. Such pre-treatment of the BCFZ442(FL) powder was necessary to comparably reduce the initial particle size to the one of the BZCY721(EL), i.e., ≈ 1.5 μm. The mixtures were then pressed into pellets and bars.

Circular pellets of 8 mm, 13 mm, and 25 mm diameters and 2-3 mm thicknesses were pressed at 100 MPa, 113 MPa, and 82 MPa, respectively, for 120 s. Green 8 mm pellets were used for sintering behavior studies. Green 13 mm pellets sintered at 800 °C, 1100 °C, and

Table 1
Powders basic characterization.

CHARACTERIZATIONS	BCFZ442	BZCY721
BET surface area (m^2/g)	6.31	7.30
Particle size (D_{50} in μm)	**3.65**	1.52
Crystal structure	Cubic	Cubic
Space group	Pm-3 m	Pm-3 m
Theoretical lattice parameter (Å)	4.14	4.23
Theoretical density in (g/cm^3)	5.84	6.20
Phase composition	Single phase with negligible $BaCO_3$ impurity	Single phase with negligible $BaCO_3$ impurity

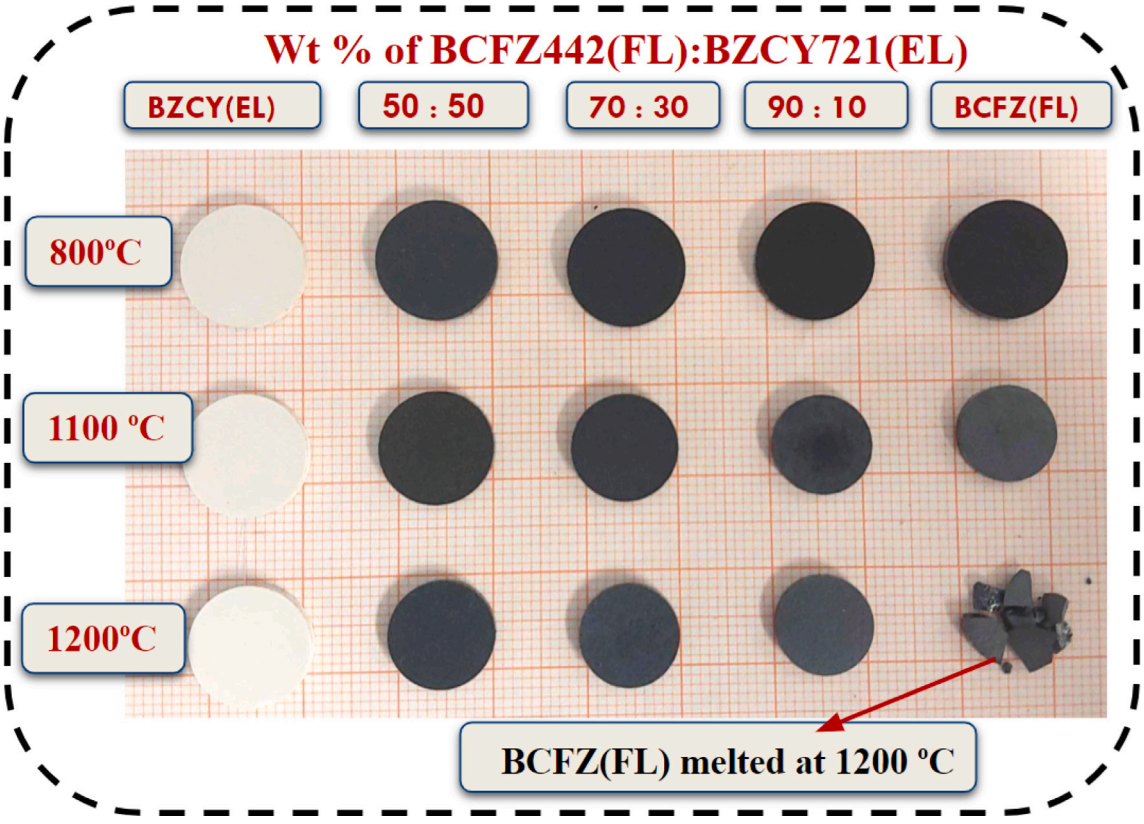

Fig. 1. Samples used for chemical compatibility study at various sintering temperature by XRD analysis.

1200 °C for 5 h were used for XRD, relative density determination, DC conductivity, and Vicker's hardness measurements.

The square bars of 5 × 5 × 25 mm^3 used for the measurement of coefficient of thermal expansion (CTE) were prepared by uniaxial pressing (P/0/Weber, Germany) with (100 MPa, 120 s) followed by cold isostatic pressing (CIP) (EPSI International, Belgium) at 200 MPa for 120 s. These samples were sintered at 1200 °C for 5 h with heating and cooling rates of 2 K/min in air atmosphere at ambient pressure.

2.3. Characterization techniques

XRD: Room temperature XRD (RT-XRD) analyses were conducted on 13 mm pellets both in the green state and after sintering at 800 °C, 1100 °C, and 1200 °C. In situ or High temperature ((HT-XRD) analysis was carried out on green 13 mm pellets from 700 °C to 1100 °C at 50 °C intervals using Cu K_α radiation (45 kV, 40 mA) on an Empyrean instrument in a 2θ range of 15–90° with a step size of 0.026° and 250 s data collection time. Rietveld refinement with the TOPAS [56] program (Bruker AXS) determined lattice parameters of crystalline phases.

Mechanical tests: Green 25 mm pellets sintered at 1100 °C for 5 h were used for measuring bending strength and elastic constant using a ring-on-ring setup following DIN EN 1288-1. Vickers hardness (Innovatest FALCON 603) was determined following ASTM standard E384-22. However, the calculation of fracture toughness was not possible due to non-uniform crack lengths.

SEM and TEM analysis: Microstructural analysis was performed on polished cross-sections using scanning electron microscopy (ApreoS, HRSEM). The cross-sections were prepared by embedding the samples in epoxy resin and allowing them to harden for 48 h before grinding and polishing up to a final polishing step of 50 nm SiO_2. The Electron transparent lamellae were prepared from the pellets using a JEOL JIB 4601 focused ion beam (FIB) system. The Scanning transmission electron microscopy (STEM) measurements were carried out, using a double aberration corrected JEOL JEM-2200FS equipped with a 200 kV field emission gun.

Thermal analysis: A thermo-gravimetric-differential thermal analysis (TG-DTA) was performed to investigate the decomposition behavior of the as-received and composite powders using a Netzsch STA 449F3 Jupiter. These composite powders were used to prepare samples of different sizes for various characterization, Fig. 1. The CTE measurements were carried out on sintered bars using NETZSCH DIL402C dilatometer.

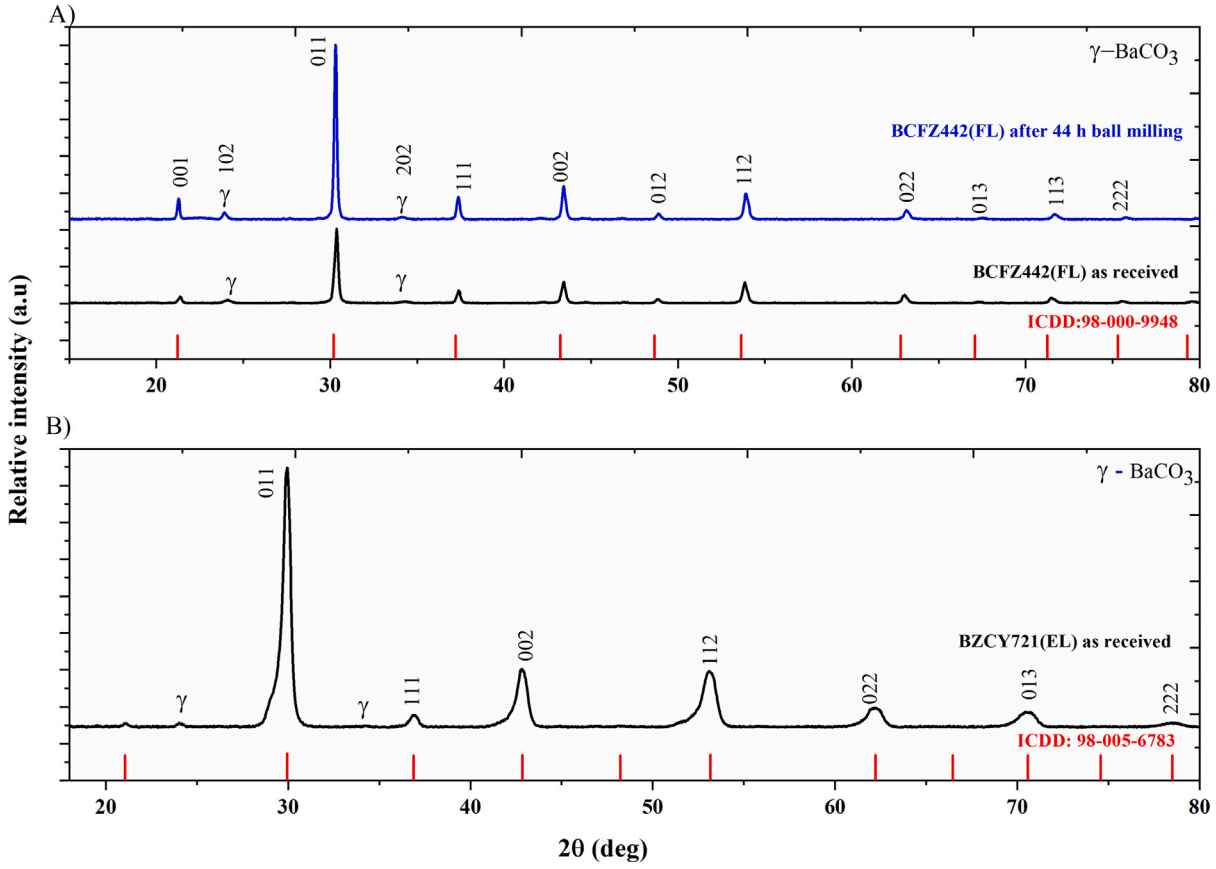

Fig. 2. XRD of (A) BCFZ442(FL) powder as received and after ball milling and (B) as received BZCY721(EL) powder with reference peak positions for both phases.

DC conductivity and activation energy: The DC conductivity and activation energy were determined using Ohm's law (equation S4) and Arrhenius equation (equation S5) while heating samples from 400–700 °C at 100 °C intervals in ambient air. A fixed current density of 0.5 A/cm^2 was applied and resulting voltages were measured. Pellets were coated on both sides with Pt paste and connected to Pt mesh current collectors in pseudo-four-point mode to eliminate Pt wire resistances.

Relative density: The relative density of sintered samples was determined using the Archimedes method with isopropanol (density of 0.786 g/cm^3 at 20 °C), assuming theoretical densities of 5.84 g/cm^3 for BCFZ442(FL) and 6.20 g/cm^3 for BZCY721(EL). The Pellets were submerged in isopropanol for 5 h to ensure uniform saturation.

3. Results and discussion

3.1. X-ray diffraction

Fig. 2 shows the X-ray diffraction (XRD) patterns of the used starting powders. As shown in Fig. 2A, the diffraction peaks recorded for the as-received BCFZ442(FL) are shifted slightly (0.2 °) towards higher angles compared to the reference peaks positions for $BaZrO_3$. This shift indicates a decrease in the lattice parameters due to the substitution with cobalt (Co) and iron (Fe) at the B-sites in the crystal structure [47, 49]. Minor peaks at 23.6° and 33.86° are observed in the XRD of the as supplied powder, corresponding to trace impurities of barium carbonate denoted as γ ($BaCO_3$, Witherite - ICDD: 98-011-0918). Ball milling of BCFZ442(FL) decreased particle size from approximately 3.65 μm to 1.44 μm. The phase composition remained unchanged.

The XRD of the as-received BZCY721(EL) powder (Fig. 2b) closely matches that of barium cerium oxide ($BaZr_{0.9}Ce_{0.1}O_3$, reference code ICDD: 98-005-6783). However, it also exhibits additional peaks corresponding to $BaCO_3$ impurities. The particle size of BZCY721(EL) is approximately 1.52 μm.

3.2. Thermal analysis

3.2.1. TG-DTA

Fig. 3 shows TG-DTA curves of BCFZ442(FL), BZCY721(EL), and mixtures of these compositions in weight fractions of 90:10, 70:30, and 50:50. The solid lines represent the mass loss (TGA curve), and the dotted lines represent the heat change (DTA curve). The TGA curves recorded for the two reference compounds differ significantly with larger mass loss registered for the BCFZ442(FL) material. This suggests that the BCFZ442(FL) component undergoes stronger thermal effects in the range of 50 °C to 1400 °C, including decomposition. As seen from the figure, three successive, distinct regions of mass loss are depicted corresponding to a total mass loss of 8.09%, 7.78%, 5.24%, 4.52%, and 1.20% for the BCFZ442(FL), BCFZ:BZCY (90:10, 70:30, 50:50) and BZCY721(EL), respectively. This indicates a strong negative linear relationship, where the mass loss decreases as the BZCY721(EL).

The first region of mass loss, accompanied by a small endothermic peak at 250 °C, can be attributed to the desorption of impurities and residual solvents. This includes the removal of physically adsorbed and absorbed water from the ethanol used during ball milling, as well as from the surrounding environment, along with CO_2. The second region (250–750 °C) and the third region (above 750 °C) of mass loss indicate increased activity related to lattice oxygen loss within these

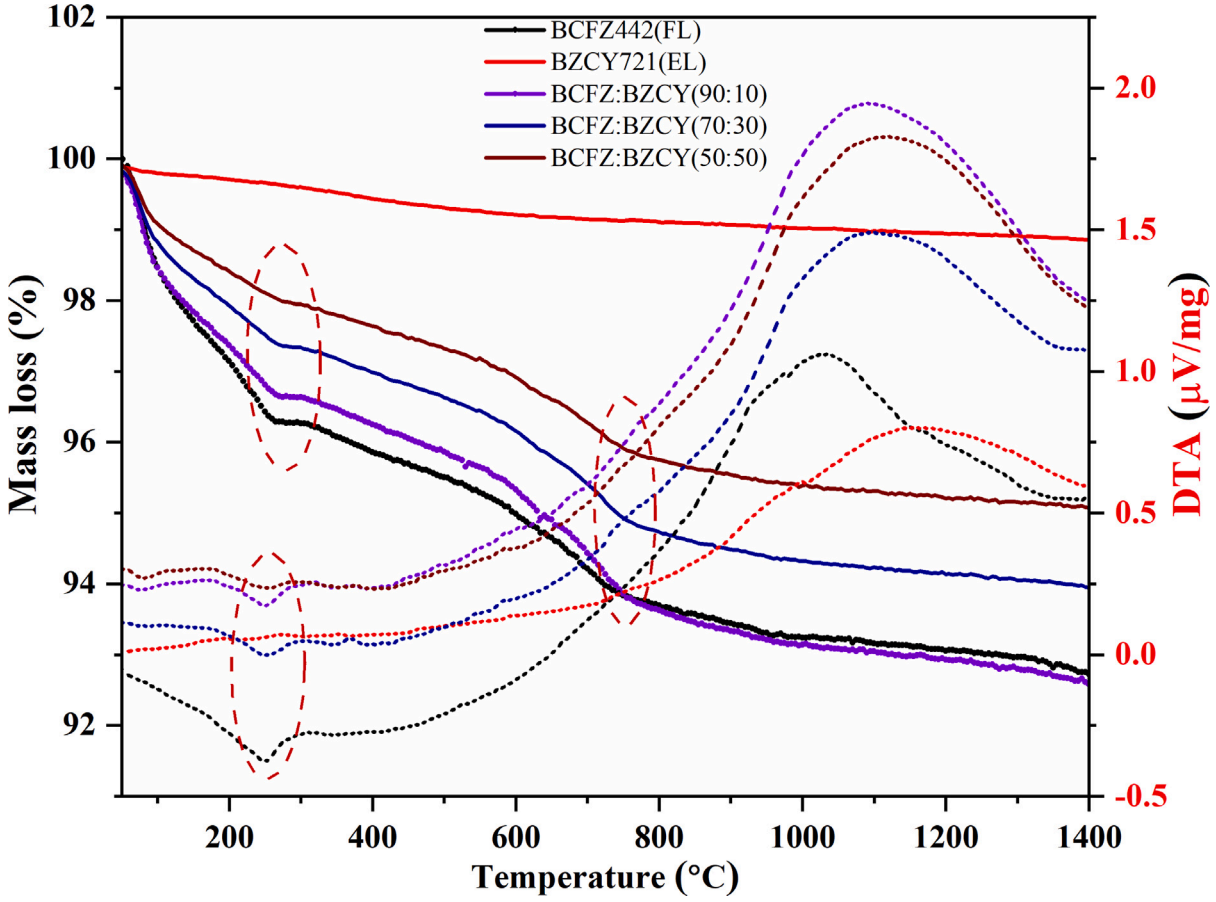

Fig. 3. Mass loss in % as a function of the temperature (solid lines) and the DTA signal in μV/mg (dotted lines) recorded by means of TG-DTA for the three composite samples with the two pristine samples as reference.

temperature ranges. This loss is associated with the thermally induced release of oxygen from the lattice and the formation of oxygen vacancies. It is accompanied by changes in the valence states of Co^{4+}/Co^{3+} and Fe^{4+}/Fe^{3+} ions between 250–750 °C, as well as Co^{3+}/Co^{2+} and Fe^{3+}/Fe^{2+} ions above 750 °C, to maintain electrical neutrality (Eqs. (1) and (2)) [57,58]. Additionally, the third region of mass loss may also be associated with inter-diffusion or elemental substitution, which compensates for the mass loss, resulting in relatively smaller mass loss at higher temperatures.

$$2Co_{Co}^{\cdot} + O_o^x \leftrightarrow 2Co_{Co}^x + V_0^{\cdot\cdot} + \frac{1}{2}O_2 \uparrow \quad (1)$$

$$2Fe_{Fe}^{\cdot} + O_o^x \leftrightarrow 2Fe_{Co}^x + V_0^{\cdot\cdot} + \frac{1}{2}O_2 \uparrow \quad (2)$$

In the given expression, $V_0^{\cdot\cdot}$ and O_o^x denote an oxide ion vacancy and an oxide ion on its regular lattice position. So, the equilibrium in Eqs. (1) and (2) shifted to the right, followed by mass loss increases.

3.2.2. Thermal expansion

Fig. 4 shows CTE curves of BCFZ442(FL), BZCY721(EL), and their mixtures in varying weight ratios. The average CTE values (depicted in Fig. 4) of the pristine samples within the 400–900 °C temperature range are similar to previously reported values [53,54].

We assume that the composite coefficient of thermal expansion (CTE) is a weighted average of the CTEs of the electrode and electrolyte materials. At a given temperature, this relationship is expressed as:

$$CTE_{comp} = CTE_{BCFZ442(FL)} \times V_e + CTE_{BZCY721(EL)} \times V_{el} \quad (3)$$

where V_e and V_{el} represent the volume percentages of the electrode and electrolyte, respectively. Please refer supplementary section for more information.

The calculated CTE values are as follows:

$CTE_{90:10}$ = 17.79E−06 K^{-1} $CTE_{70:30}$ = 15.78E−06 K^{-1} $CTE_{50:50}$ = 13.73E−06 K^{-1}

The experimentally obtained average CTE values align closely with those predicted by the rule of mixtures, following a linear trend ($y = 0.10x + 8.38$), as illustrated in Fig. 5. The observed CTE behavior of BZCY721 closely resembles that of $Ba_{1.015}Zr_{0.625}Ce_{0.2}Y_{0.175}O_{3-\delta}$ as reported by Deibert et al. [59] The appearance of the shallow region (a region of a subtle dip) may be associated with the dehydration which can lead to chemical shrinkage [54,60,61]. The average CTE difference between pristine samples BCFZ442(FL) and BZCY721(EL) is ≈ 124%. This difference is reduced as the weight fraction of BZCY721(EL) increases and reaches its minimum for the BCFZ: BZCY(50:50) composition. BCFZ: BZCY(50:50) has nearly constant thermal expansion within the 400–900 °C temperature range. In contrast, other compositions exhibit an inflection in thermal expansion between 450–600 °C similar to literature [51]. The appearance of inflection and its magnitude can be attributed to the loss of lattice oxygen and the formation of oxygen vacancies as noticed in Fig. 3. Furthermore, this is accompanied with the reduction of B-site cations Co and Fe from + 4 to + 3 to maintain electrical neutrality (Eqs. (1), (2)) [62,63]. The loss of lattice oxygen reduces the electrostatic attraction between B-cations and oxygen, increasing the size of BO_6, consequently enhances the lattice expansion [57,58]. The effect is clearly noticed for the 70:30 and 90:10 composites, as well for the pristine BCFZ442 material.

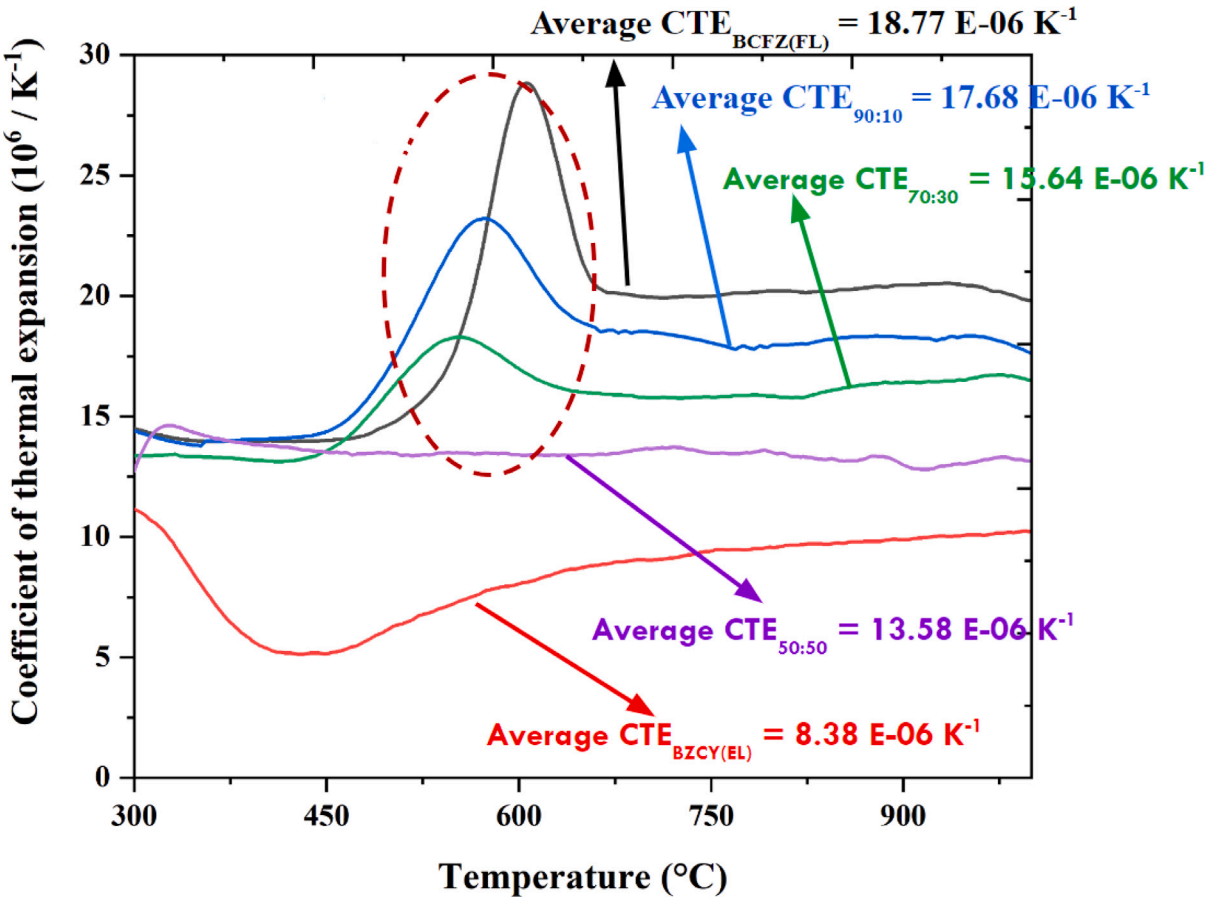

Fig. 4. Thermal expansion of the developed composite materials with BCFZ442 and BZCY721 pristine materials given as a reference.

These significant CTE differences during heating and cooling may contribute to the development of thermomechanical stresses within the functional layer and could induce delamination between layers. Gradual compositional changes may help to maintain cell integrity.

3.2.3. Sintering behavior and relative density

Understanding the sintering behavior of both pristine and composite materials is crucial for determining the optimal sintering temperature of a functional layer. Fig. 6 depicts the densification curve of pristine and composite green samples with varying weight fractions of BCFZ442(FL) and BZCY721(EL). As expected, due to its inherently higher sintering temperature (T ≥ 1600 °C), BZCY721(EL) shows very limited densification and influences the overall sintering behavior of the composites. This is reflected in the figure, where the onset temperature of densification increases with increasing weight percentages of BZCY721(EL), (The onset temperature is determined by the intersection point of extrapolated tangents drawn to the initial linear portions of the sintering curves). For BCFZ442(FL), densification begins at a relatively low temperature of 923 °C and is completed between 1200 to 1300 °C. In contrast, BZCY721(EL) exhibits a much higher onset temperature of 1170 °C. The composite samples, BCFZ:BZCY (90:10, 70:30, and 50:50), display a gradual increase in onset temperature with increasing BZCY721(EL) content, ranging from 983 °C to 1090 °C. The minor peak observed at 246 °C in the BCFZ442(FL) based materials curves (but not for the BZCY721) likely corresponds to the change in surface composition lead to densification. The step observed at a higher temperature (1335 °C) in the BZCY721(EL) curve can be attributed to change in the densification mechanism. Based on these observations, the optimal sintering temperature for the functional layer, depending on the BCFZ fraction, should be above 983 °C, the lowest observed onset temperature among the composites. This ensures sufficient densification/porosity while avoiding excessively high temperatures that could harm the material properties.

The porosity of the functional layer should closely match that of the steam electrode typically in the range, between 25% and 40% [64]. Fig. 7 shows the variation of relative density experimentally determined for pristine and composite samples with varying weight fractions of BCFZ442(FL) and BZCY721(EL). The initial variation of relative density is quite normal which is because of different compaction behavior of powders. The samples were sintered at three different temperatures, i.e., 800 °C, 1100 °C, and 1200 °C. The relative density was determined using the Archimedes experimental setup. Fig. 7 indicates that the relative density of the composites increases with temperature. However, BCFZ442(FL) stands out by achieving maximum relative density of 97% at 1100 °C. Above this temperature, the sample melted as result of oversintering (see Fig. 1) and its density dropped. This behavior is primarily attributed to microstructural changes, such as possibly excessive grain growth, grain boundary weakening, associated porosity or cracks, that occur due to prolonged exposure to high temperatures during sintering. The relative density of BZCY721(EL) remains significantly lower and shows minimal change with temperature, suggesting very poor densification at this condition, in line with the previous analysis section (Fig. 6). The porosities of BCFZ442(FL) and BCFZ:BZCY(90:10, 70:30 and 50:50), at 1100 °C are calculated to be 3%, 10%, 27%, 37%, and 44%, respectively. These values demonstrate the ability to tailor the porosity of the functional layer through compositional variation and adjusting the sintering temperature.

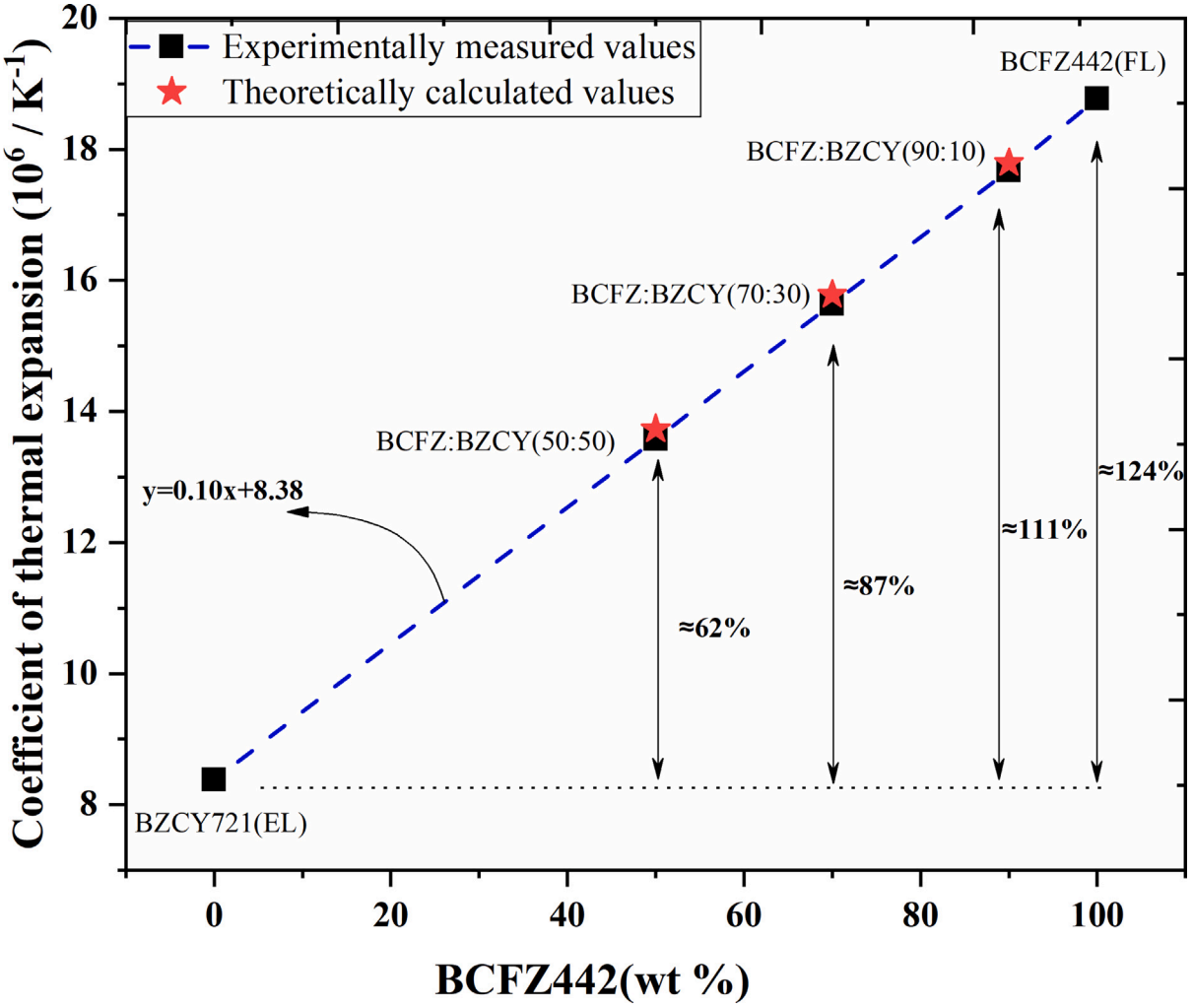

Fig. 5. Comparison of experimentally measured CTE with theoretically calculated CTE.

3.3. Chemical compatibility of BCFZ442 and BZCY721

A comparative analysis of X-ray diffraction (XRD) pattern was performed on three composites: Fig. 8A) BCFZ: BZCY (90:10) (B) BCFZ: BZCY (70:30) (C) BCFZ: BZCY (50:50), heat treated at various temperatures, i.e., 800 °C, 1100 °C, and 1200 °C. Despite the fact that the operation windows of BCFZ:BZCY based cells will not be extending towards such high temperatures, the basic exploration and characterization of their interactions such treatments are essential to control their fabrication process (including sintering study) but no addition reaction and phase detected formation. Interestingly, Fig. 8 shows a shifting of prominent XRD peaks from lower angles to higher angles above 800 °C. To determine the intermediate temperature of reversal in lattice size, the HT-XRD was performed. The resulting HT-XRDs of the in situ heat-treated composite mixtures were compared to their corresponding thermally non-treated references. The significant peak shifts of XRD peak's positions of all composition towards smaller angles which indicate the lattice expansion As clearly seen from Fig. 9. From the HT-XRD data lattice parameters of the two phases constituting the composites could be evaluated based on Rietveld refinement and compared to those of the thermally non-treated reference materials. Fig. 10 presents the compositional dependence of the lattice parameter as a function of temperature.

The left part of the figure shows the lattice parameters of pristine BCFZ442 and BZCY721 and the individual constituents in the composite materials at RT differ, e.g., increased, possibly due to lattice parameter mismatch which can induce lattice strain in one or both phases upon mixing. This strain can cause the lattice to expand, leading to an observed increase in the lattice parameter. Furthermore, the right part of the figure shows several trends:

1. A change in the slopes of the curves observed at 950 °C for all samples suggesting the turning point in elemental interdiffusion and the threshold of the thermo-chemical compatibility between the two phases;
2. Lattice parameter of the BZCY721 phase in composites starts decreasing around and above the equi-weight ratio of the phases and this trend is stronger at higher temperatures where the interdiffusion is more pronounced (top portion of the graph);
3. For the BCFZ442 phase in composites the opposite trend to (ii) is observed (top portion of the graph): the lattice expands with increasing the amount of BZCY721 over the temperature. Comparing the lattice parameters for BCFZ442 pristine versus the BCFZ442 in the 50:50 composite at e.g., 1100 °C, one can clearly see that this difference is quantitatively 4–5 times larger than in the case of the BZCY721 pristine versus the BZCY721 in the 50:50 composite. This observation confirms that the BZCY721 is

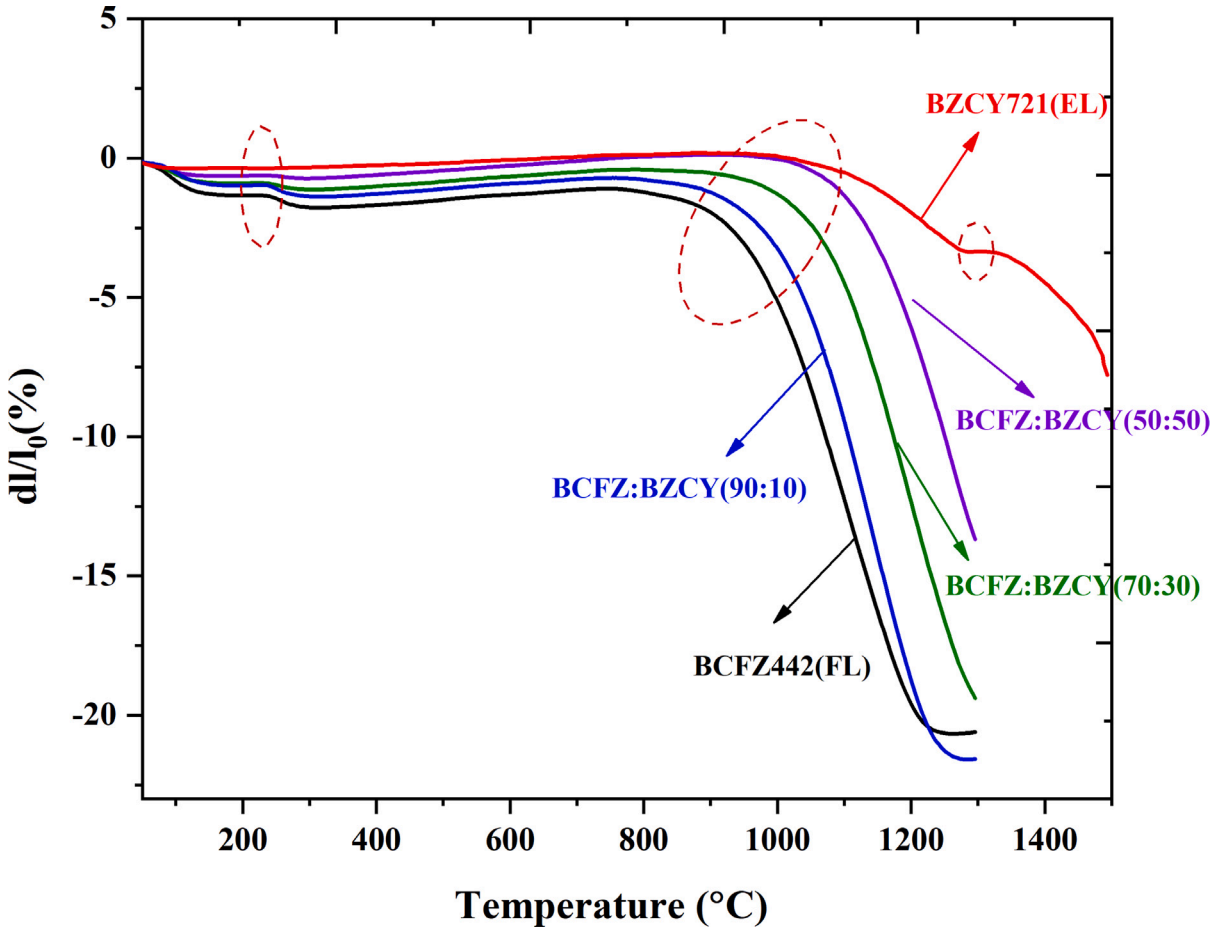

Fig. 6. Sintering behavior: shrinkage in % recorded as a function of the temperature for composite materials with different BCFZ442 to BZCY721 fractions.

less affected by the interdiffusion than the BCFZ442 phase. In the context of (ii) and (iii), the lattice parameter of the BCFZ442(FL) phase in BCFZ: BZCY (70:30, 50:50) composites tend towards the lattice parameter of BZCY721(EL) as the weight fraction of BZCY721(EL) increases. This can be because of the diffusion of larger cations (Ce^{4+}, Y^{3+}) from the BZCY721(EL) phase into the BCFZ442(FL) lattice. Conversely, the lattice parameter of BZCY721(EL) in BCFZ: BZCY (90:10, 70:30) composites shows a sudden decrease, approaching the lattice parameter of BCFZ442(FL). This effect can be attributed to the diffusion of cations with comparatively smaller ionic radii (Co^{3+}, Fe^{3+}) from the BCFZ442(FL) phase into the BZCY721(EL) lattice, which needs to be proven by high resolution characterization.

These observations suggest that for this type of ceramic composites the optimal treatment temperature has to be below 950 °C in order to keep pronounced lattice expansion or contraction and interdiffusion as limited as possible. When comparing the results from the HT-XRD with the XRDs recorded at RT on heat treated and cooled down samples, there are some differences that are briefly outlined (Fig. 8). The blue dotted vertical lines in the pattern indicate the peak position corresponding to the BZCY721(EL) phase, while the red lines represent the BCFZ442(FL) peaks. As seen most pronouncedly in the position of the strongest peaks recorded for the composites, there is a shift towards lower angles for sample heat treated at 800 °C. Above 800 °C, these peaks shift back towards higher angles. The observed behavior of initial expansion and subsequent contraction of the crystal lattice at temperatures higher than 800 °C, can be attributed to pronounced inter-diffusion. Notably, the BZCY721(EL) phase becomes dominant in the BCFZ:BZCY (50:50) composite above 800 °C. Furthermore, these peaks overlap significantly at 1100 °C and 1200 °C. Such a peak overlap is not observed in the other composites and it suggests a higher propensity for inter-diffusion phenomena in the BCFZ: BZCY (50:50) composite, potentially prohibiting its use as functional layer. So, the weight percent of BZCY721(EL) in composites should be less than 50%. For samples treated at high sintering temperatures, lattice expansion caused by the loss of lattice oxygen can also be taken into account as it will reduce the electrostatic attraction between B-cations and oxygen, increasing the size of BO_6.

The γ-denoted peak in the reference XRD, attributed to the impurity $BaCO_3$, disappears with increasing the temperature. This suggests $BaCO_3$ decomposition into BaO and CO_2 between 800 °C and 1200 °C.

3.4. Microstructure and phase analysis

Fig. 11 and Fig. 12 show the SEM-EDS analysis result for the BCFZ:BZCY(70:30) and BCFZ:BZCY(50:50) composites sintered at 1100 °C, respectively. The agglomeration of material is observed at the micrometer level, likely due to the manual mixing process of the composite powders. This agglomeration may introduce non-uniformity in the material distribution, potentially affecting the absolute measured values. Nevertheless, the relative comparisons between the different composites remain reliable. The BCFZ: BZCY (70:30) composite exhibits a dual-phase microstructure with evident porosity and inter-diffusion.

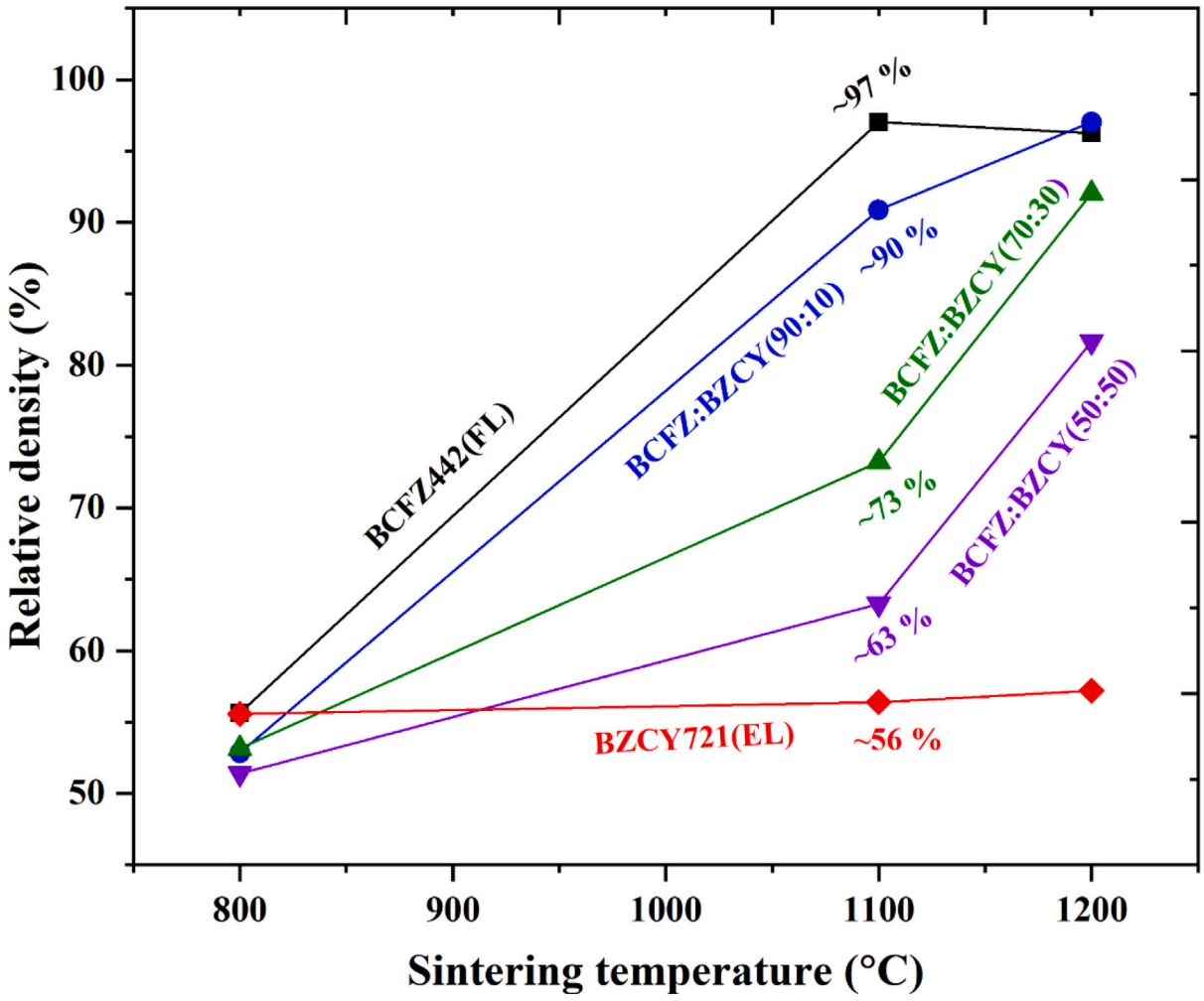

Fig. 7. Relative density of composite samples with pristine samples as reference (data points are connected by solid lines for comparison purposes).

A dual-phase microstructure with enhanced percolation enhances bulk triple-phase boundaries (TPBs), which reduces the activation energy and increases the electrocatalytic activities. In contrast, the BCFZ:BZCY (50:50) composite shows a significantly higher degree of inter-diffusion. This extensive inter-diffusion forms a mixed phase, suggesting a degree of chemical instability within the material. The presence of the mixed phase is also supported by the complementary STEM measurements of a BCFZ:BZCY (50:50) composite sintered at 1100 °C.

STEM EDS investigations (Fig. 13A) reveal the co-localization of significant amounts of cobalt and iron in the same grain as yttrium and cerium. The high-resolution STEM image in Fig. 13 reveals the presence of well-defined grain boundaries separating adjacent crystalline grains of mixed phase. These grains exhibit orientations along specific crystallographic directions, as indicated by the labels [111] and [102] in the image. The average lattice spacings were determined to be 0.409 nm and 0.419 nm for the red and cyan areas in the top and bottom of the image, respectively, corresponding to the [102] and [111] orientations. Considering the ±5% measurement accuracy of STEM, the average lattice spacing (0.414 nm) of the mixed phase is in good agreement with the theoretical average lattice spacing (0.419 nm) of the host materials. This suggests that the mixed phase retains the same crystal structure as the host materials.

However, the presence of this mixed phase may be detrimental to the conductivity of the material. It can potentially hinder the hopping of electrons, thereby impeding electrical transport. This observation aligns with the findings from the compatibility analysis based on in-situ HT-XRD and RT-XRD, which revealed significant peak overlap for the BCFZ:BZCY (50:50) composite sintered at 1100 °C and 1200 °C, indicating a higher propensity for inter-diffusion in this composition.

3.5. Conductivity

The perovskite BCFZ442 is a mixed conductor, its total conductivity includes both electronic and ionic, i.e., protonic and oxygen ionic contributions, owing to the presence of electron holes, protons and oxygen vacancies. However the ionic conductivity is approximately two orders of magnitude lower than the electronic conductivity [57,65]. Therefore, it is reasonable to assume that the measured conductivity values primarily reflect the electronic conductivity. Fig. 14 illustrates the conductivity variation of composite materials at sintering temperatures of 800 °C, 1100 °C, and 1200 °C. Fig. 15 depicts the temperature dependence of DC electrical conductivity (Arrhenius plots) of composite materials measured in the 400–700 °C range in air. The general trend observed is that the conductivity of all tested material increases with increasing the temperature that is in accordance to the semiconductor behavior. Notably, amongst all composites BCFZ:BZCY(90:10) and BCFZ:BZCY(70:30) sintered at 1100 °C show maximum conductivity. In contrast, BCFZ: BZCY (50:50) exhibits expectedly the lowest conductivity across the measured range, reaching a maximum in the

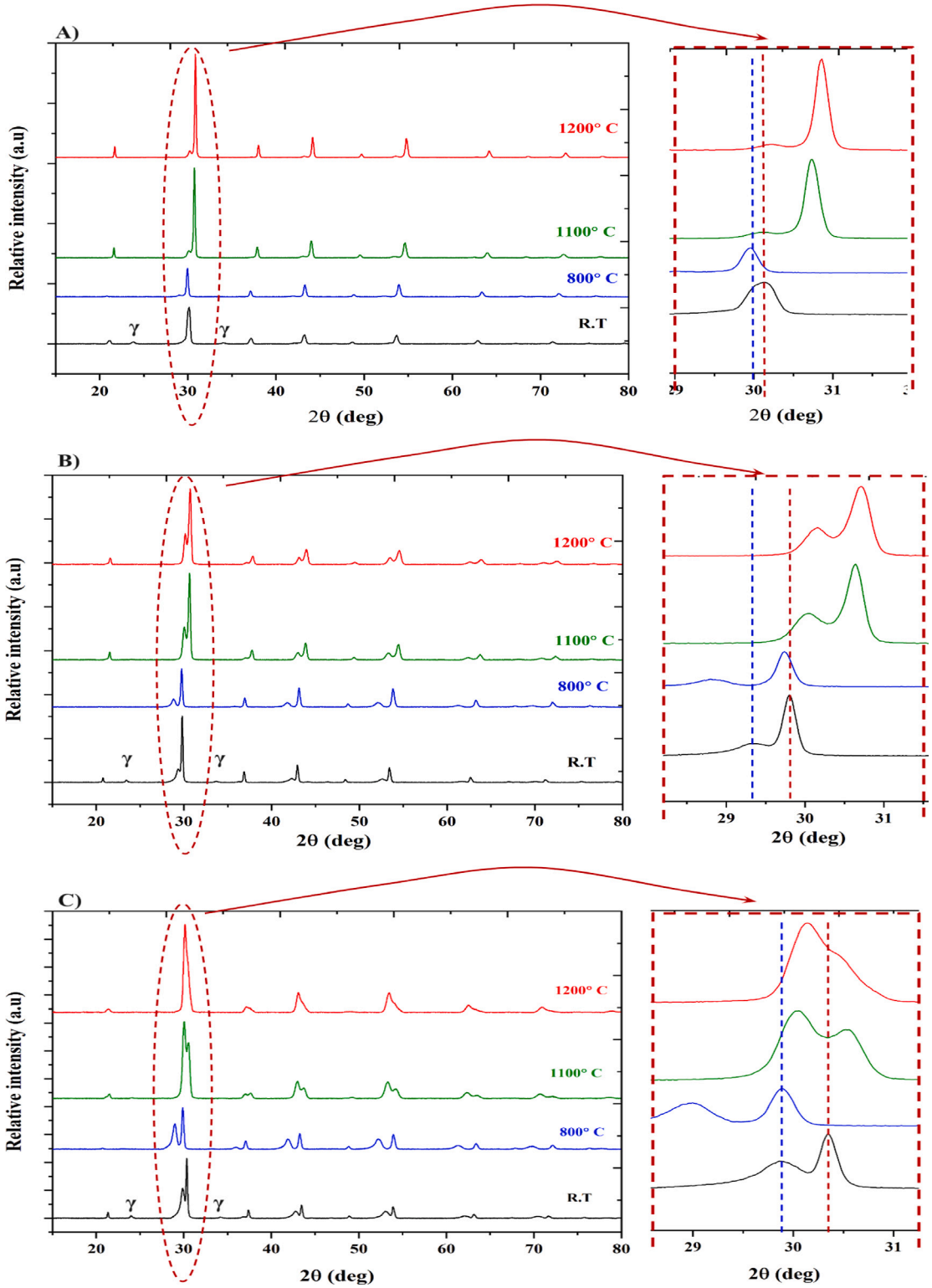

Fig. 8. Comparison of XRD recorded at RT of (A) BCFZ:BZCY(90:10), (B) BCFZ:BZCY(70:30) and (C) BCFZ:BZCY(50:50) sintered at different temperatures and cooled down to RT. XRDs of the untreated mixtures are given as a reference.

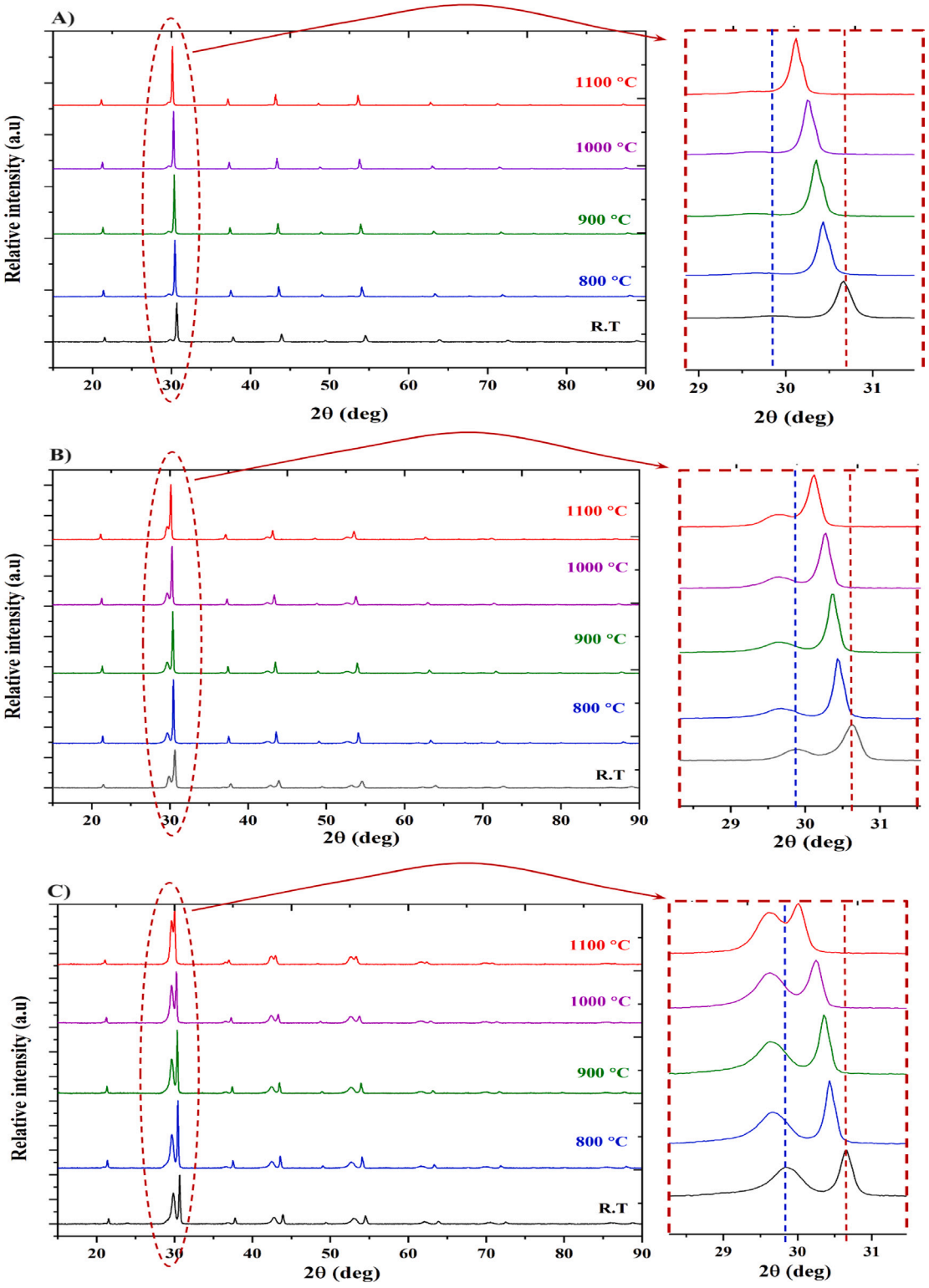

Fig. 9. Comparison of HT-XRD of (A) BCFZ:BZCY(90:10) (B) BCFZ:BZCY(70:30) (C) BCFZ:BZCY(50:50) sintered at different temperatures with room temperature XRD as reference.

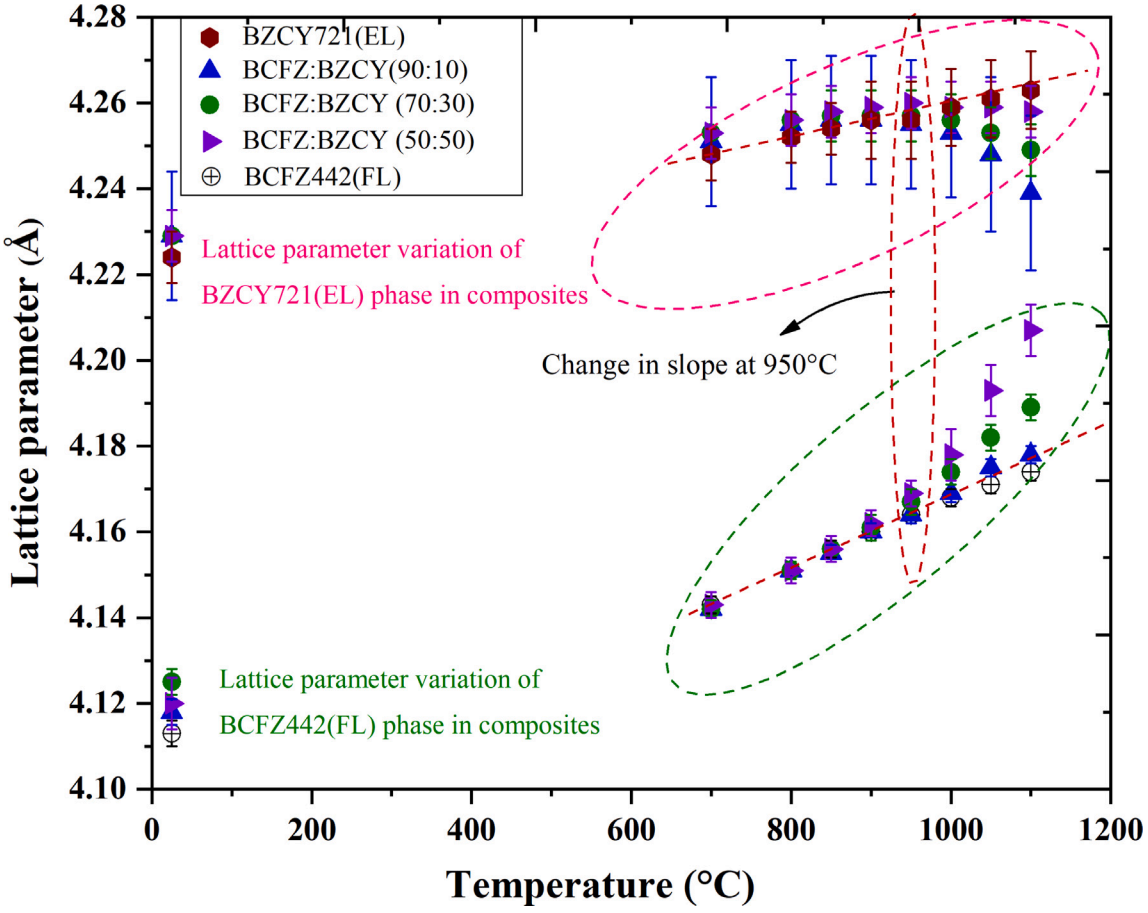

Fig. 10. Lattice parameter variations of the composites' constituting individual phases BCFZ442(FL) and BZCY721(EL) with temperature.

compound sintered at 1200 °C. Table 2 summarizes the conductivity and activation energy data. The activation energy was calculated from the slope of the curves (ln(σ) vs. 1000/T). As observed from Fig. 15, the conductivity of BCFZ442(FL) sintered at 1100 °C exhibits a pronounced change in the slope at around 500 °C (15b). From Table 2, the transition from a rapid increase (E_a = 0.39 eV) to a less steep rise with lower activation energy (E_a = 0.12 eV) is similar to what was reported by [50,51,66]. This suggests a change in the conductivity mechanism, possibly due to a change in the type and concentration of charge carriers. The average activation energy for BCFZ442 (0.23 eV) aligns well with previous reports [67]. In contrast to this composition, BCFZ:BZCY (50:50) sintered at 800 °C has an opposite transition at 550 °C from a less steep rise (E_a = 0.04 eV) to a rapid increase with higher activation energy (E_a = 0.22 eV). This change in the slope is commonly associated with the formation of oxygen vacancies and the reduction of Co^{4+}/Fe^{4+} to Co^{3+}/Fe^{3+} [51,62,68,69] as a compensation mechanism.

Analyzing furthermore the data in the Table 2, few trends are observed in the 600 °C-temperature dependence of the electrical conductivity. (It is important to note that the reference data for BCFZ442 presented in the existing literature may not be directly applicable due to variations in powder synthesis techniques, sample preparation methods, and sintering conditions employed in different studies):

1. When more BZCY721 is added, the composite conductivity decreases for all three sintering series (horizontal dependence in the table). The activation energy for the materials sintered at 800 °C shows an incremental trend. However, for specimens sintered at 1100 °C, it is lowest with 30% of BZCY721. This drop in E_a could be attributed to an optimal balance of both phases, which can improve reaction sites and, ultimately, enhance mixed ionic–electronic conductivity. Additionally, at the highest temperature, the activation energy among the compositional series reduces with a decrease in the BCFZ442 content in the composite.
2. As the sintering temperature increases for one composition, a peak conductivity value is recorded at 1100 °C (vertical dependence in the table). The average activation energy follows an incremental trend from the lowest to the highest sintering temperature (0.126 eV for the 50:50 composite sintered at 800 °C), with an exception noted for the 70:30 composite (0.13 eV).

3.6. Mechanical properties

Mechanical properties like elastic modulus, bending strength, and hardness are crucial factors for these composites, as they are designed to function as a layer or interlayer between the electrolyte and the steam electrode in proton ceramic electrolysis cells (PCEC). These materials must possess adequate strength to endure thermal, chemical, and mechanical stresses during operation, as well as withstand contact loading during stacking. Fig. 16 illustrates the compositional dependence of Vickers hardness for various materials sintered at 1100 °C, while Fig. 17 shows their elastic modulus and bending strength. These mechanical properties vary based on the porosity of the materials, as discussed in several studies [70–74]. For instance, elastic modulus can be expressed using the equation $E = E_0(1\text{-}ap)^n$, as proposed by Phani

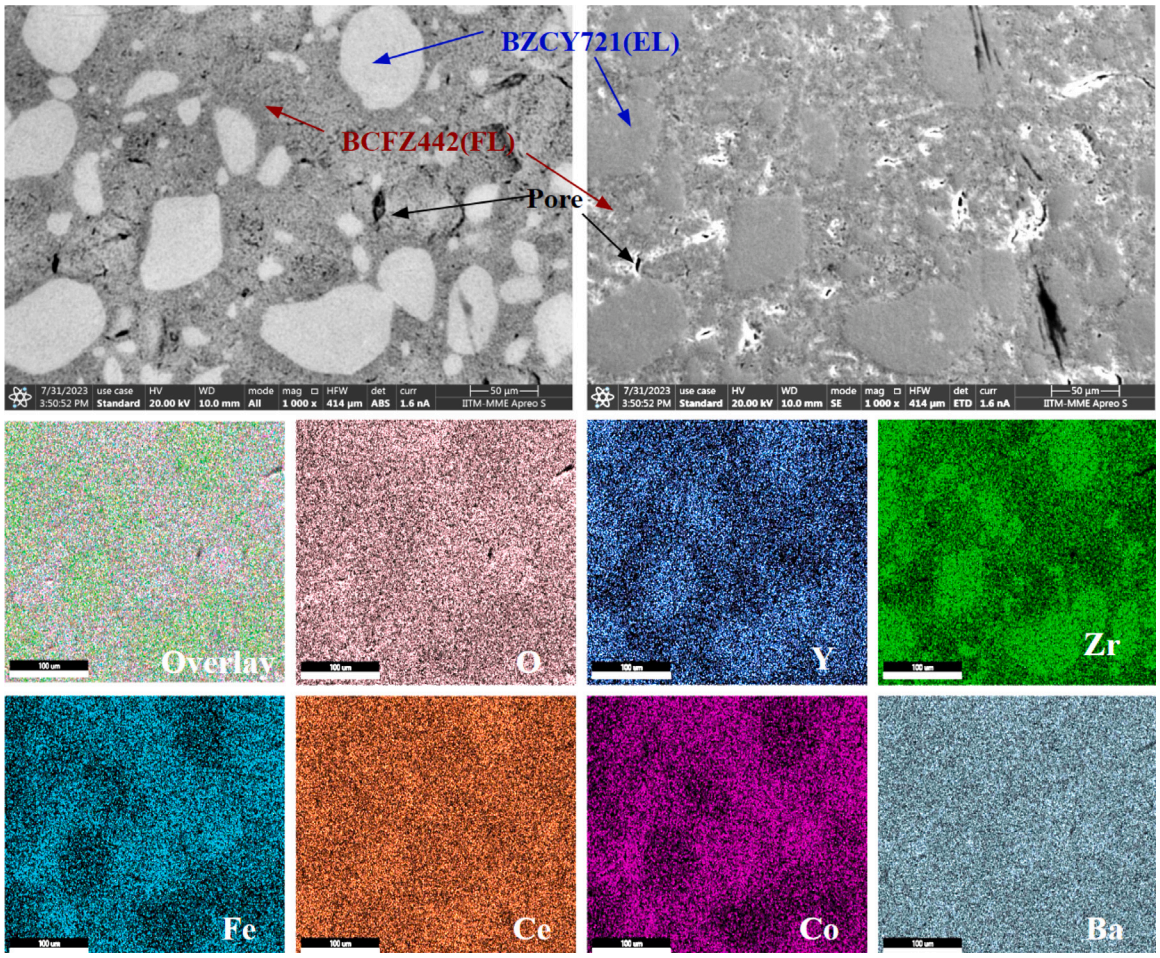

Fig. 11. SEM micrographs (in backscattered electron imaging and secondary electron imaging modes) and energy dispersive x-ray (EDS) mapping of BCFZ:BZCY (70:30) heat treated at 1100 °C.

Table 2
Conductivity at 600 °C in air and the corresponding activation energy calculated from the Arrhenius plots for composite samples sintered at various temperatures.

Sintering T (°C)	Conductivity (S/cm) at 600 °C					
	BCFZ442(FL)	BCFZ:BZCY composites			Ref. BCFZ442	Reference
		90:10	70:30	50:50		
800 °C	0.42	0.27	0.05	0.01	< 1.95 (sintered at 900 °C)	[50]
1100 °C	1.17	0.70	0.35	0.07	> 2.09 (sintered at 1050 °C)	[51]
1200 °C	–	0.49	0.26	0.09	2.71 (sintered at 1270 °C)	[66]
E_a (eV)						
800 °C	0.12	0.15	0.16	0.04, 0.22	< 0.18, 0.06 (sintered at 900 °C)	[50]
1100 °C	0.39, 0.12	0.18	0.13	0.17	> 0.37, 0.24 (sintered at 1050 °C)	[51]
1200 °C	–	0.34	0.26	0.19	0.11, 0.04 (sintered at 1270 °C)	[66]

and Yound et al. [74]. In this equation, the material constant "a" represents the "packing geometry factor", with values ranging from 1 to 3.85, while the constant "n" depends on grain morphology and pore geometry. However, this relation was not validated in this study as it falls outside its scope.

Analysis of Figs. 16 and 17 indicates that BCFZ442(FL) exhibits superior hardness, bending strength, and elastic modulus compared to BZCY721(EL). This difference is primarily due to the varying sintering temperatures of these materials. The sintering temperature used here (1100 °C) is lower than the typical densification onset temperature (1170 °C) for BZCY721(EL). Consequently, increasing the weight fraction of BZCY721(EL) in the composite leads to cracks and porosity, thereby reducing its overall mechanical properties. It is also important to note that the manual mixing process of the composite powders may have introduced some non-uniformity in material distribution, potentially affecting the absolute measured values. However, the relative comparisons between the different composites remain reliable. Additionally, the higher bending strength, elastic modulus, and hardness of BCFZ:BZCY (70:30) compared to BCFZ:BZCY (50:50) underscore its potential as a suitable material for this application.

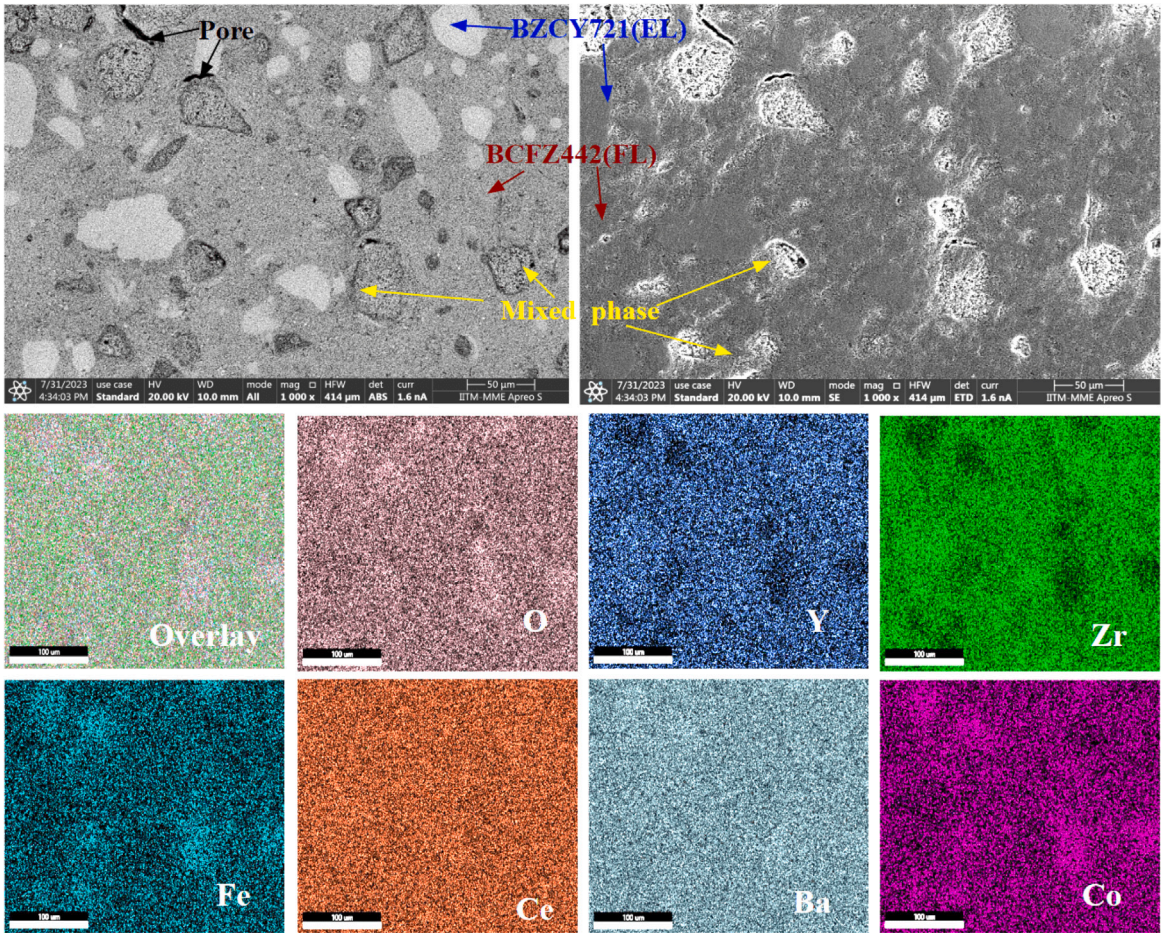

Fig. 12. SEM micrographs (in backscattered electron imaging and secondary electron imaging modes) and energy dispersive x-ray (EDS) mapping of BCFZ:BZCY (50:50) heat treated at 1100 °C.

4. Summary and conclusions

This study investigates the development of a composite steam electrode for PCECs to address limitations caused by poor interface contact with the electrolyte. The steam electrode reaction mechanisms in PCECs differ from those in SOECs/SOFCs, rendering the typical air electrode materials unsuitable for PCECs. Material selection and properties tailoring for PCEC steam electrodes is crucial, balancing cost-effectiveness with performance. A common approach to improve the electrode performance and interface contact with the electrolyte involves the design of composite electrodes of two ceramic phases: the electrode and the electrolyte [54]. In this study ceramic–ceramic composites were developed, consisting of Co and Fe-rich $BaZrO_3$ (BCFZ442) and a typical proton conducting material BZCY721. The objective was to identify the optimal material composition and the corresponding fabrication conditions for optimal microstructure, compatibility, and adhesion with the electrolyte. Three composites compositions were developed and systematically investigated, namely 90:10, 70:30, and 50:50 - BCFZ442:BZCY721 and their properties were compared to the reference pristine materials (see Fig. 18).

Our results indicate that within the PCEC operating temperature range, BCFZ442 undergoes a more substantial thermal effect (mass loss) compared to BZCY721. Additionally, a significant CTE mismatch (124%) and a CTE inflection observed in BCFZ442 render the pristine material incompatible with the electrolyte at operating temperatures. This mismatch may contribute to the development of thermomechanical stresses within electrode layer and could induce delamination between layers. This inflection and magnitude are attributed to the formation of oxygen vacancies accompanied by the reduction of B-site cations (Co and Fe) from +4 to +3 (to maintain electrical neutrality) likely also contributes to the observed mass loss. The addition of BZCY721 mitigates both mass loss and the CTE mismatch, with the 50:50 composition exhibiting the lowest mismatch.

A key challenge identified is the difference in sintering temperatures between BCFZ442 (onset at 923 °C, maximum density at 1200 °C) and BZCY721 (onset at 1170 °C). Room temperature X-ray diffraction (RT-XRD) analysis revealed initial lattice expansion and contraction, indicating interdiffusion above 800 °C. HT-XRD analysis of in-situ heat-treated composites suggests a threshold of thermal-compatibility between the phases at 950 °C. This temperature minimizes interdiffusion. Peak overlapping observed in the 50:50 composition (where BZCY721 becomes the primary phase) suggests lattice parameter convergence between BCFZ442 and BZCY721. Microstructural analysis revealed a well-defined dual-phase microstructure for the 70:30, indicative of phase stability. In contrast, the 50:50 composite exhibited a more complex microstructure with an additional, unquantified mixed phase. STEM-EDS analysis identified significant co-localization of cobalt and iron with yttrium and cerium within this mixed phase, suggesting a higher degree of interdiffusion in the 50:50 composition compared to the 70:30 counterpart. This observation aligns with the findings

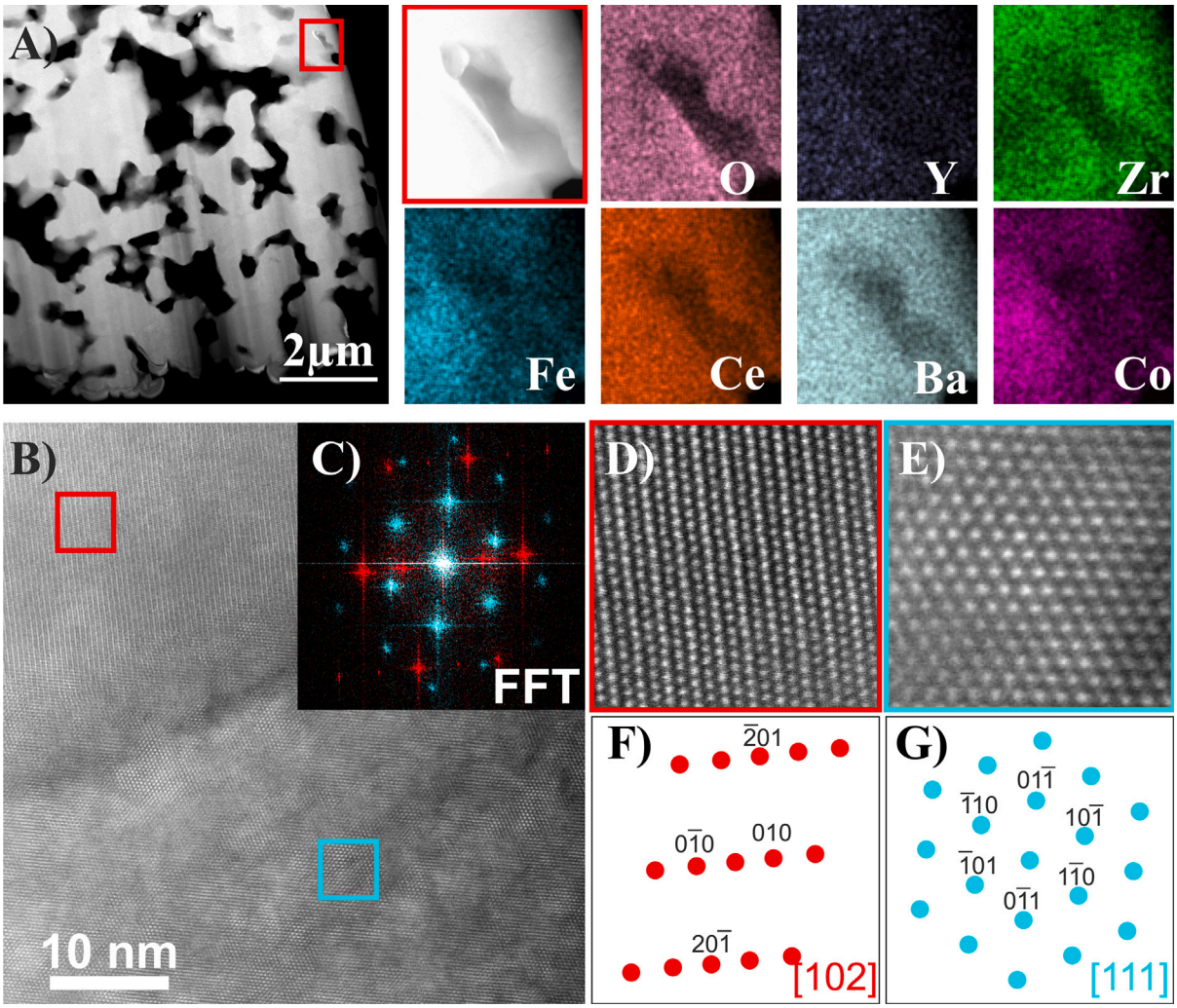

Fig. 13. (A) EDS mapping via STEM of a lamella (marked by the red square box) in a BCFZ:BZCY (50:50) sample sintered at 1100 °C. (B) High-resolution HAADF STEM image of a grain boundary between a [102] (top, red) and a [111] oriented grain (bottom, cyan). The corresponding Fast Fourier transformation (FFT) is shown in (C) , in which the spots belonging to each grain are highlighted in the respective color. (D) and (E) depict higher magnification images of the respective grains. The corresponding indexed diffraction patterns are shown in (F) and (G), respectively.

from the compatibility analysis (e.g., in-situ XRD, RT-XRD), which likely indicates a thermodynamic driving force for increased interdiffusion at this specific compositional ratio. The formation of a mixed phase makes it chemically incompatible and compromises the desired functional properties of the 50:50 composite. DC conductivity analysis corroborated these findings, with conductivity decreasing as the weight fraction of BZCY721 increased, reaching a minimum at 50:50. All compositions (except 50:50) achieved maximum conductivity at 1100 °C, exhibiting semiconducting behavior with increasing conductivity at higher temperatures. However, the activation energy generally increased with temperature. Notably, the 70:30 composition displayed the lowest activation energy (0.13 eV) at 1100 °C (similar as reported by [47,53,75]), indicating an increase in the number of reaction sites (triple phase boundaries - TPBs).

In conclusion, our study suggests that a 70:30 BCFZ442:BZCY721 weight ratio is the best composition among the tested ones for a functional layer material due to its improved interface contact with the electrolyte. The 30% BZCY content effectively mitigates the CTE inflection observed in BCFZ442, promoting lattice stability and a desirable dual-phase microstructure. Furthermore, the 70:30 composite exhibits the lowest activation energy, indicating increased reaction sites (triple phase boundaries) for enhanced performance. While a sintering temperature of 1100 °C introduces minimal inter-diffusion, this limited interaction appears to favor proton hopping, as evidenced by the highest conductivity and lowest activation energy observed at this temperature for the 70:30 composition. Additionally, compared to the 50:50 composite sintered at 1100 °C, the 70:30 composition demonstrates superior mechanical properties such as hardness, elastic modulus, and fracture strength. Conversely, lowering the sintering temperature would not provide sufficient thermal energy for complete sintering of BZCY (onset temperature: 1170 °C), potentially compromising the mechanical stability of the microstructure. Therefore, a trade-off exists between minimizing inter-diffusion for enhanced electrical conductivity and ensuring mechanical structure stability. Based on these considerations, we recommend a sintering temperature of 1100 °C for the 70:30 functional layer composition. However, for the overall steam electrode, a lower temperature of 950 °C is recommended to maintain optimal phase compatibility.

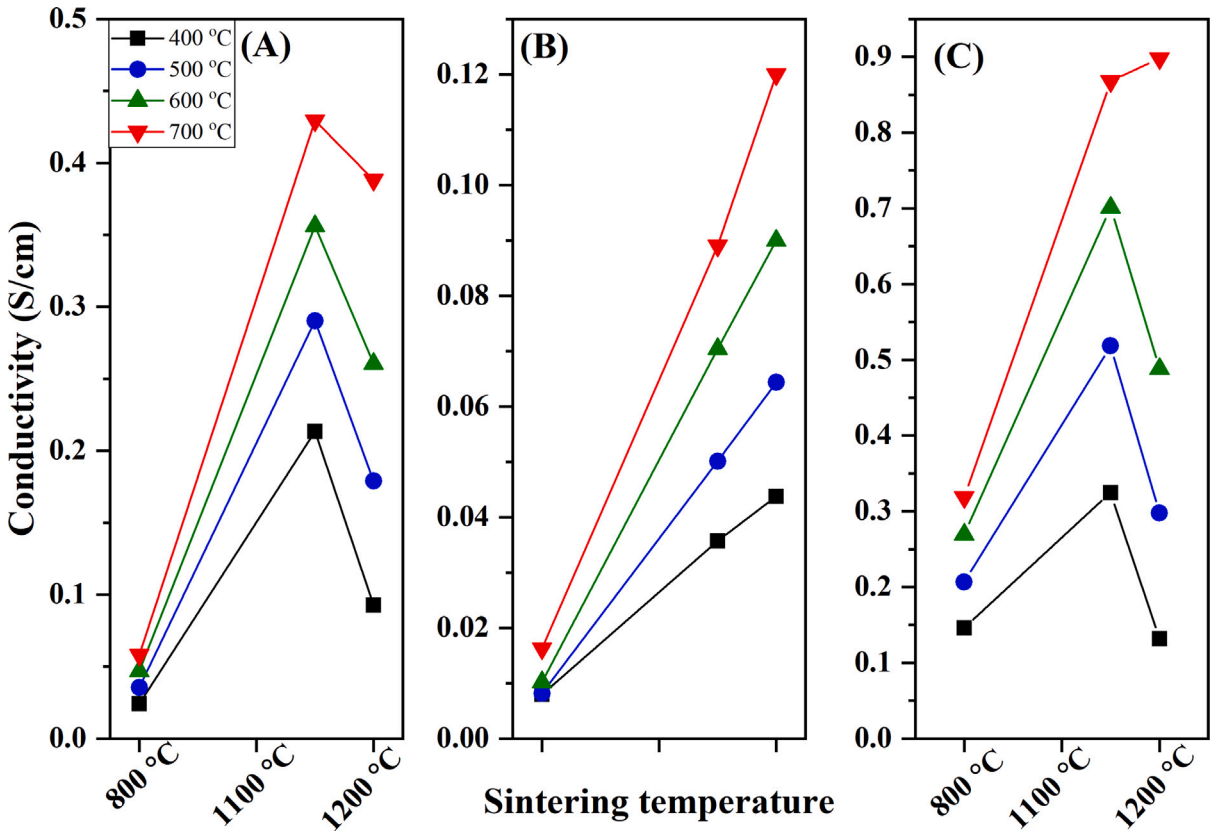

Fig. 14. Conductivity variations with sintering temperatures of composite samples at (A) BCFZ: BZCY(70:30), (B) BCFZ: BZCY(50:50) and (C) BCFZ: BZCY(90:10) (data points are connected by solid lines for comparison purposes).

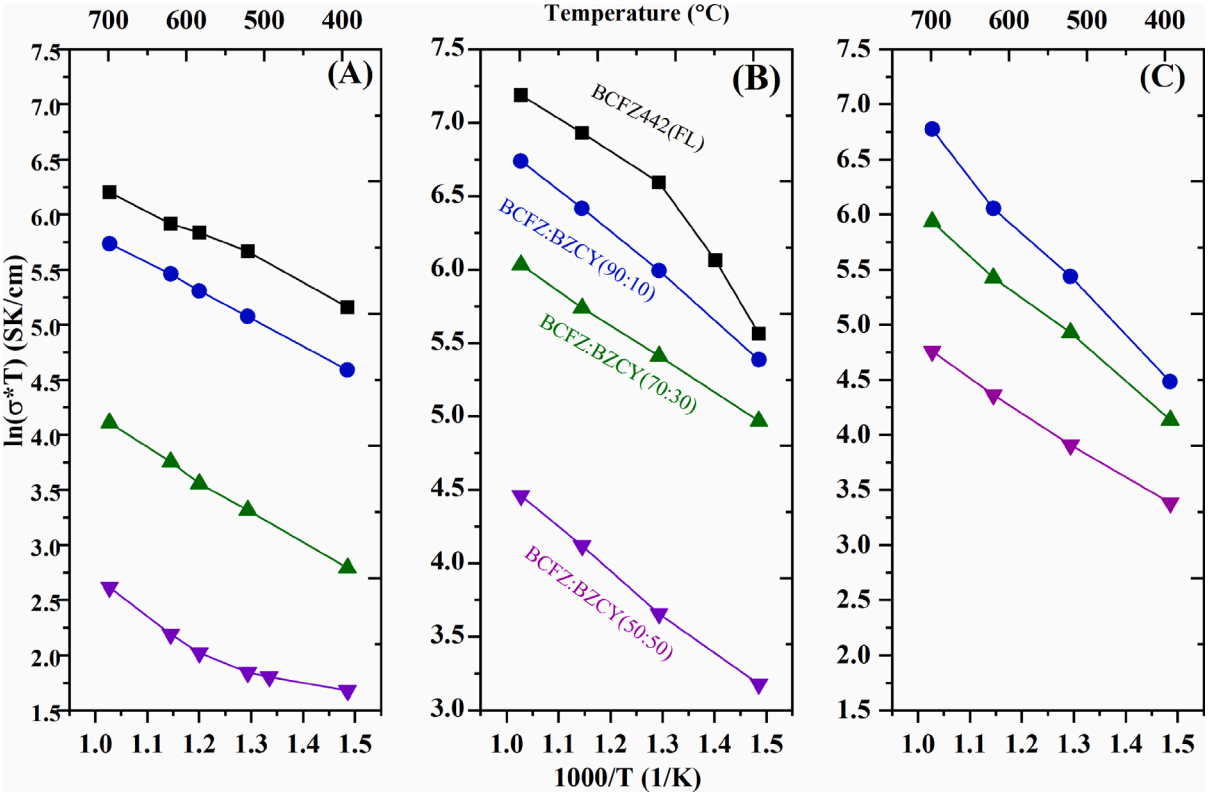

Fig. 15. Temperature dependence of the DC conductivity (Arrhenius plots), plotted for composite samples sintered at (A) 800 °C, (B) 1100 °C and (C) 1200 °C (selected data points are displayed for comparison. For additional details, please refer to the supplementary file.).

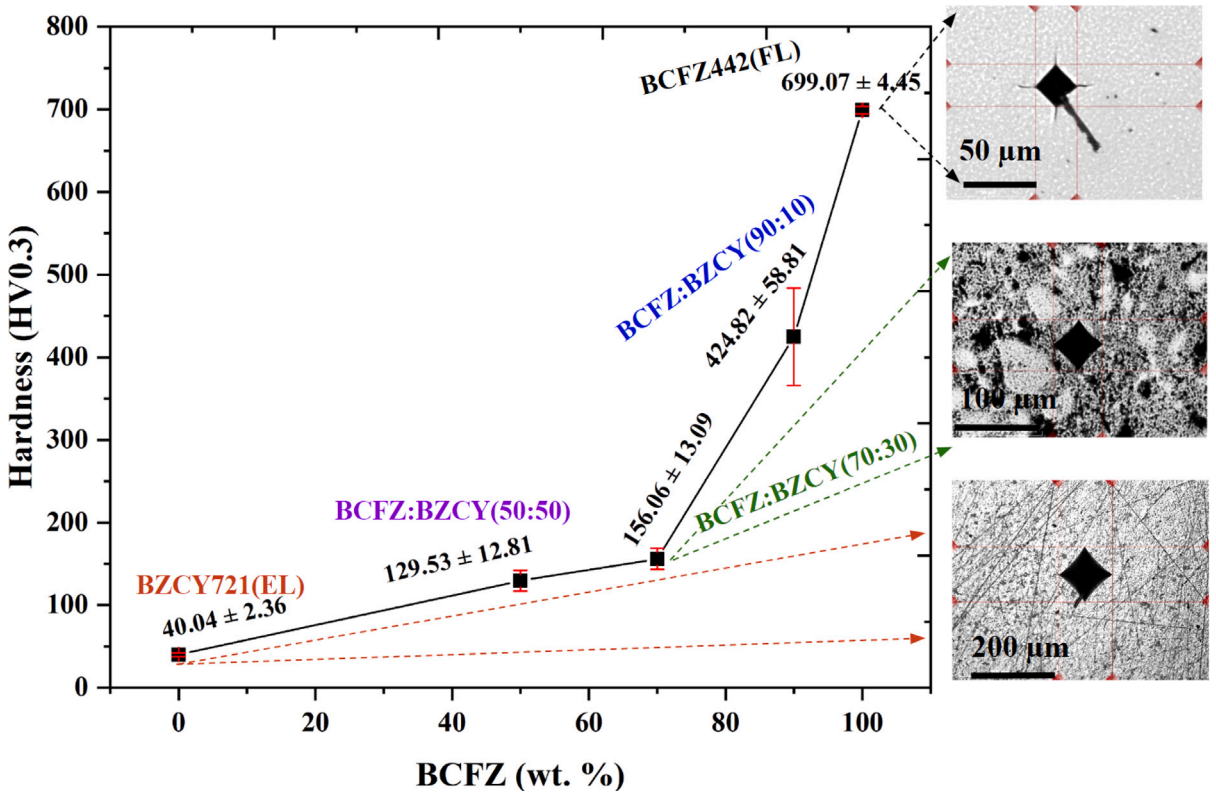

Fig. 16. Compositional dependence of the Vickers's hardness determined for pristine and composite samples sintered at 1100 °C with their corresponding indentation micrographs.

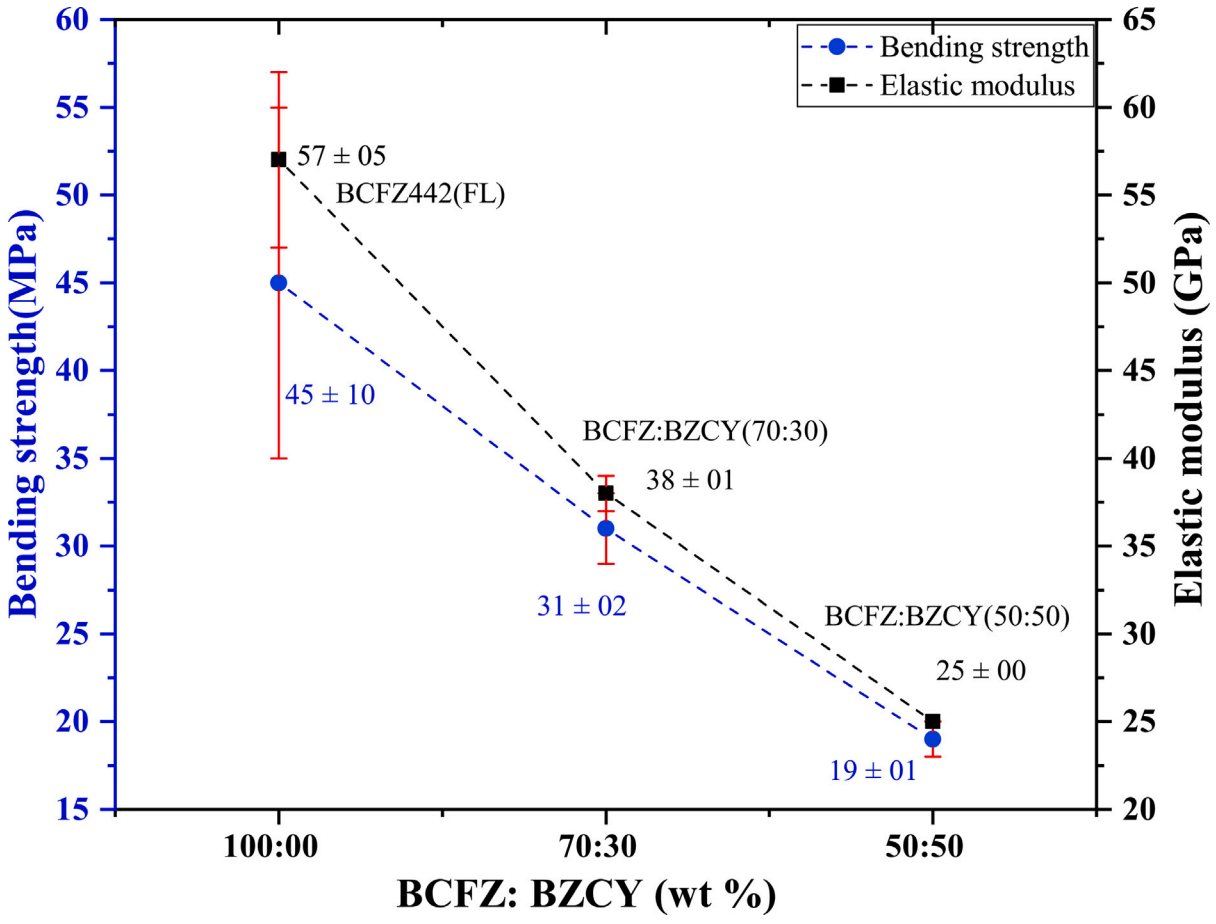

Fig. 17. Bending strength and elastic modulus of pristine materials and BCFZ442:BZCY721 composites sintered at 1100 °C.

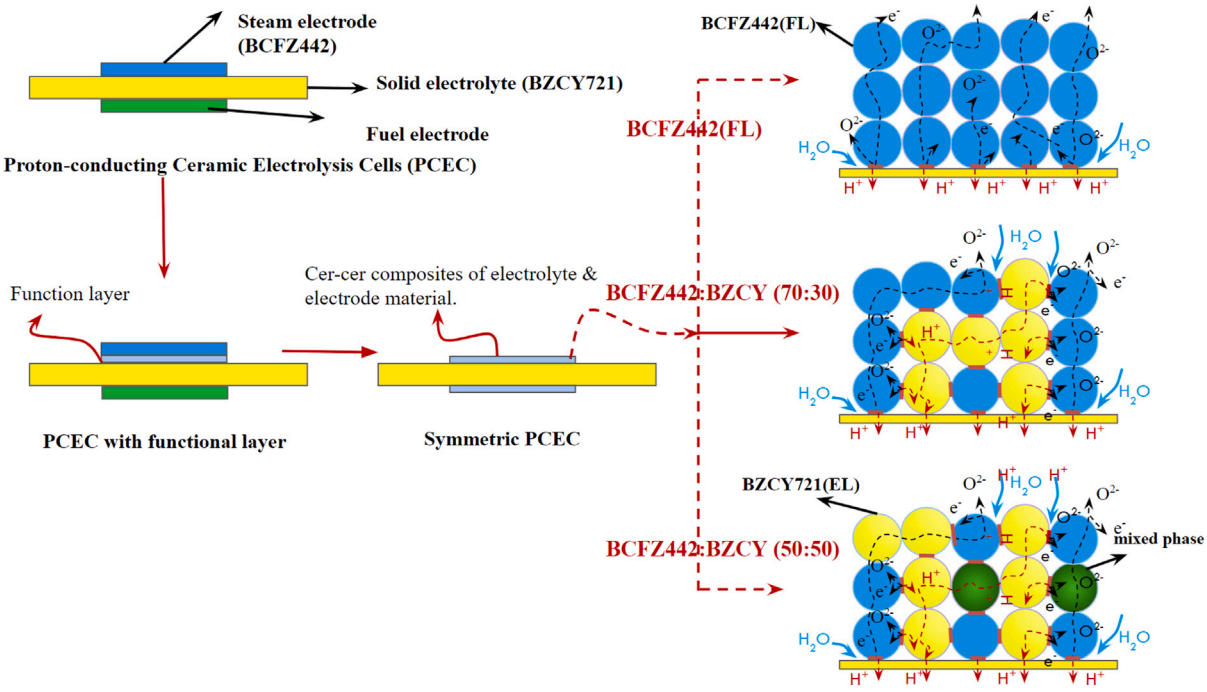

Fig. 18. Left: Schematic depicting the introduction of a functional layer between the electrolyte and the steam electrode. Right: Schematic illustrating the particle network of a pristine steam electrode (BCFZ442) and a composite steam electrode (70:30 and 50:50).

CRediT authorship contribution statement

Shivam Kumar Dwivedi: Writing – original draft, Visualization, Methodology, Investigation, Formal analysis, Conceptualization. **Laura-Alena Schaefer:** Writing – review & editing, Supervision, Resources, Investigation, Conceptualization. **Yuan Zeng:** Writing – review & editing, Supervision, Resources. **Yoo Jung Sohn:** Writing – review & editing, Formal analysis. **Jürgen Malzbender:** Writing – review & editing, Resources. **Andreas Beyer:** Writing – review & editing, Formal analysis. **Celina Becker:** Investigation. **Kerstin Volz:** Supervision. **Norbert H. Menzler:** Writing – review & editing, Supervision, Resources, Funding acquisition. **Olivier Guillon:** Writing – review & editing, Supervision, Project administration, Funding acquisition. **Mariya E. Ivanova:** Writing – review & editing, Supervision, Resources, Project administration, Formal analysis, Conceptualization. **Ravi Kumar:** Writing – review & editing, Supervision, Resources, Funding acquisition.

Declaration of competing interest

The authors declare that they have no known competing financial interests or personal relationships that could have appeared to influence the work reported in this paper.

Acknowledgments

We gratefully acknowledge the Junior Research Fellowship from IIT Madras-RWTH Aachen University and the Graduate research grant received from the Indo-German Centre for Sustainability. The Helmholtz Association of German Research Centers (HGF) and the Federal Ministry of Education and Research (BMBF), Germany are gratefully acknowledged for supporting the development of H_2 generation technologies within the frame of the Innovation Pool project "Solar H_2: Highly Pure and Compressed" and the Helmholtz Research Program "Materials and Technologies for the Energy Transition" (MTET). The publication is also funded by the German Research Foundation (Deutsche Forschungsgemeinschaft DFG) - 491111487. Open Access funding enabled and organized by project DEAL. We also thank Mr. Ankit Bansal, Dr. Raghunath Sharma, and Dr. Abha Bharati from the Laboratory for High-Performance Ceramics, IIT Madras as well as Dr. Muhammed Shirjeel Khan and the technicians from IMD-2, Forschungszentrum Jülich GmbH, for their valuable support and technical discussions.

Appendix A. Supplementary data

Supplementary material related to this article can be found online at https://doi.org/10.1016/j.jeurceramsoc.2025.117348.

References

[1] International Energy Agency, Electricity 2024 - Analysis and forecast to 2026, IEA Publication, Paris, 2024.

[2] L. Bi, S. Boulfrad, E. Traversa, Steam electrolysis by solid oxide electrolysis cells (SOECs) with proton-conducting oxides, Chem. Soc. Rev. 43 (2014) 8255–8270, http://dx.doi.org/10.1039/C4CS00194J.

[3] L. Lei, J. Zhang, Z. Yuan, J. Liu, M. Ni, F. Chen, Progress report on proton conducting solid oxide electrolysis cells, Adv. Funct. Mater. 29 (37) (2019) 1903805, http://dx.doi.org/10.1002/adfm.201903805.

[4] S.H. Jensen, C. Graves, M. Mogensen, C. Wendel, R. Braun, G. Hughes, Z. Gao, S.A. Barnett, Large-scale electricity storage utilizing reversible solid oxide cells combined with underground storage of CO_2 and CH_4, Energy Env. Sci. 8 (2015) 2471–2479, http://dx.doi.org/10.1039/C5EE01485A.

[5] M.E. Ivanova, R. Peters, M. Müller, S. Haas, M.F. Seidler, G. Mutschke, K. Eckert, P. Röse, S. Calnan, R. Bagacki, et al., Technological pathways to produce compressed and highly pure hydrogen from solar power, Angew. Chem. Int. Ed. 62 (32) (2023) e202218850.

[6] Y. Tian, H. Zheng, L. Zhang, B. Chi, J. Pu, J. Li, Direct electrolysis of CO_2 in symmetrical solid oxide electrolysis cell based on $La_{0.6}Sr_{0.4}Fe_{0.8}Ni_{0.2}O_{3-\delta}$ electrode, J. Electrochem. Soc. 165 (2) (2018) F17, http://dx.doi.org/10.1149/2.0351802jes.

[7] S.D. Ebbesen, S.H. Jensen, A. Hauch, M.B. Mogensen, High temperature electrolysis in alkaline cells, solid proton conducting cells, and solid oxide cells, Chem. Rev. 114 (21) (2014) 10697–10734, PMID: 25283178. http://dx.doi.org/10.1021/cr5000865.

[8] K.-D. Kreuer, Proton-conducting oxides, Annu. Rev. Mater. Res. 33 (1) (2003) 333–359.

[9] C. Duan, J. Huang, N. Sullivan, R. O'Hayre, Proton-conducting oxides for energy conversion and storage, Appl. Phys. Rev. 7 (1) (2020) 011314, http://dx.doi.org/10.1063/1.5135319.

[10] E. Vøllestad, R. Strandbakke, M. Tarach, D. Catalán-Martínez, M.-L. Fontaine, D. Beeaff, D.R. Clark, J.M. Serra, T. Norby, Mixed proton and electron conducting double perovskite anodes for stable and efficient tubular proton ceramic electrolysers, Nat. Mater. 18 (7) (2019) 752–759.

[11] M. Balaguer, Y.J. Sohn, D. Kobertz, S. Kasatikov, A. Fantin, M. Müller, N.H. Menzler, O. Guillon, M.E. Ivanova, Characterization of Y and Mn co-substituted $BaZrO_3$ ceramics: Material properties as a function of the substituent concentration, Solid State Ion. 382 (2022) 115959.

[12] A.V. Kasyanova, L.R. Tarutina, A.O. Rudenko, J.G. Lyagaeva, D.A. Medvedev, $Ba(Ce,Zr)O_3$-based electrodes for protonic ceramic electrochemical cells: towards highly compatible functionality and triple-conducting behaviour, Russ. Chem. Rev. 89 (6) (2020) 667.

[13] D. Chuancheng, K. Robert, Z. Huayang, S. Neal, Z. Liangzhu, B. Liuzhen, J. Dylan, O. Ryan, 019/03/01 TI - Highly efficient reversible protonic ceramic electrochemical cells for power generation and fuel production, Nat. Energy 4 (1) (2019) 230–240, http://dx.doi.org/10.1038/s41560-019-0333-2.

[14] H. Iwahara, T. Esaka, H. Uchida, N. Maeda, Proton conduction in sintered oxides and its application to steam electrolysis for hydrogen production, Solid State Ion. 3–4 (1981) 359–363, http://dx.doi.org/10.1016/0167-2738(81)90113-2.

[15] K. Kreuer, Proton-conducting oxides, Annu. Rev. Mater. Res. 33 (1) (2003) 333–359, http://dx.doi.org/10.1146/annurev.matsci.33.022802.091825.

[16] T. Schober, H. Bohn, Water vapor solubility and electrochemical characterization of the high temperature proton conductor $BaZr_{0.9}Y_{0.1}O_{2.95}$, Solid State Ion. 127 (3–4) (2000) 351–360.

[17] T. Norby, M. Widerøe, R. Glöckner, Y. Larring, Hydrogen in oxides, Dalton Trans. (19) (2004) 3012–3018.

[18] S. Ricote, N. Bonanos, G. Caboche, Water vapour solubility and conductivity study of the proton conductor $BaCe_{0.9-x}Zr_xY_{0.1}O_{3-\delta}$, Solid State Ion. 180 (14–16) (2009) 990–997.

[19] B. Kiho, J.D. Young, C.H. Jong, K. Donghwan, H. Jongsup, K. Byung-Kook, L. Jong-Ho, S. Ji-Won, S.J. Hyung, Demonstrating the potential of yttrium-doped barium zirconate electrolyte for high-performance fuel cells, Nat. Commun. 8 (2017) 1723–2041, http://dx.doi.org/10.1038/ncomms14553.

[20] J. Kim, S. Sengodan, S. Kim, O. Kwon, Y. Bu, G. Kim, Proton conducting oxides: A review of materials and applications for renewable energy conversion and storage, Renew. Sustain. Energy Rev. 109 (2019) 606–618, http://dx.doi.org/10.1016/j.rser.2019.04.042.

[21] S. Hossain, A.M. Abdalla, S.N.B. Jamain, J.H. Zaini, A.K. Azad, A review on proton conducting electrolytes for clean energy and intermediate temperature-solid oxide fuel cells, Renew. Sustain. Energy Rev. 79 (2017) 750–764, http://dx.doi.org/10.1016/j.rser.2017.05.147.

[22] F.J. Loureiro, N. Nasani, G.S. Reddy, N. Munirathnam, D.P. Fagg, A review on sintering technology of proton conducting $BaCeO_3$-$BaZrO_3$ perovskite oxide materials for Protonic Ceramic Fuel Cells, J. Power Sources 438 (2019) 226991, http://dx.doi.org/10.1016/j.jpowsour.2019.226991.

[23] K. Katahira, Y. Kohchi, T. Shimura, H. Iwahara, Protonic conduction in Zr-substituted $BaCeO_3$, Solid State Ion. 138 (1) (2000) 91–98, http://dx.doi.org/10.1016/S0167-2738(00)00777-3.

[24] H. Matsumoto, T. Sakai, Y. Okuyama, Proton-conducting oxide and applications to hydrogen energy devices, Pure Appl. Chem. 85 (2) (2012) 427–435.

[25] Z. Shao, S.M. Haile, A high-performance cathode for the next generation of solid-oxide fuel cells, Nature 431 (2004) http://dx.doi.org/10.1038/nature02863.

[26] N. Bausá, C. Solís, R. Strandbakke, J.M. Serra, Development of composite steam electrodes for electrolyzers based on barium zirconate, Solid State Ion. 306 (2017) 62–68.

[27] S. Choi, S. Yoo, J. Kim, S. Park, A. Jun, S. Sengodan, J. Kim, J. Shin, H.Y. Jeong, Y. Choi, et al., Highly efficient and robust cathode materials for low-temperature solid oxide fuel cells: $PrBa_{0.5}Sr_{0.5}Co_{2-x}Fe_xO_{5+\delta}$, Sci. Rep. 3 (1) (2013) 2426.

[28] J.H. Kim, M. Cassidy, J.T. Irvine, J. Bae, Electrochemical investigation of composite cathodes with $SmBa_{0.5}Sr_{0.5}Co_2O_{5+\delta}$ cathodes for intermediate temperature-operating solid oxide fuel cell, Chem. Mater. 22 (3) (2010) 883–892.

[29] S. Takahashi, S. Nishimoto, M. Matsuda, M. Miyake, Electrode properties of the Ruddlesden–Popper series, $la_{n+1}Ni_no_{3n+1}$ (n=1, 2, and 3), as intermediate-temperature solid oxide fuel cells, J. Am. Ceram. Soc. 93 (8) (2010) 2329–2333, http://dx.doi.org/10.1111/j.1551-2916.2010.03743.x.

[30] A. Taracón, S. Skinner, R. Chater, F. Hernández-Ramırez, J. Kilner, Layered perovskites as promising cathodes for intermediate temperature solid oxide fuel cell, J. Mater. Chem. 17 (2007) 3175–3181.

[31] H. Tu, Y. Takeda, N. Imanishi, O. Yamamoto, $Ln_{0.4}Sr_{0.6}Co_{0.8}Fe_{0.2}O_{3-\delta}$ (Ln=La, Pr, Nd, Sm, Gd) for the electrode in solid oxide fuel cells, Solid State Ion. 117 (3) (1999) 277–281, http://dx.doi.org/10.1016/S0167-2738(98)00428-7.

[32] M. Koyama, C.-j. Wen, K. Yamada, $La_{0.6}Ba_{0.4}CoO_3$ as a cathode material for solid oxide fuel cells using a $BaCeO_3$ electrolyte, J. Electrochem. Soc. 147 (1) (2000) 87.

[33] C. Zuo, S. Zha, M. Liu, M. Hatano, M. Uchiyama, Ba $(Zr_{0.1}Ce_{0.7}Y_{0.2})O_{3-\delta}$ as an electrolyte for low-temperature solid-oxide fuel cells, Adv. Mater. 18 (24) (2006) 3318–3320.

[34] H. Yamaura, T. Ikuta, H. Yahiro, G. Okada, Cathodic polarization of strontium-doped lanthanum ferrite in proton-conducting solid oxide fuel cell, Solid State Ion. 176 (3–4) (2005) 269–274.

[35] H. Ding, B. Lin, X. Liu, G. Meng, High performance protonic ceramic membrane fuel cells (PCMFCs) with $Ba_{0.5}Sr_{0.5}Zn_{0.2}Fe_{0.8}O_{3-\delta}$ perovskite cathode, Electrochem. Commun. 10 (9) (2008) 1388–1391.

[36] Y. Ling, J. Yu, X. Zhang, L. Zhao, X. Liu, et al., A cobalt-free $Sm_{0.5}Sr_{0.5}Fe_{0.8}Cu_{0.2}O_{3-\delta}$–$Ce_{0.8}Sm_{0.2}O_{2-\delta}$ composite cathode for proton-conducting solid oxide fuel cells, J. Power Sources 196 (5) (2011) 2631–2634.

[37] S. Li, K. Xie, Composite oxygen electrode based on LSCF and BSCF for steam electrolysis in a proton-conducting solid oxide electrolyzer, J. Electrochem. Soc. 160 (2) (2013) F224.

[38] L. Bi, S.P. Shafi, E. Traversa, Y-doped $BaZrO_3$ as a chemically stable electrolyte for proton-conducting solid oxide electrolysis cells (SOECs), J. Mater. Chem. A 3 (11) (2015) 5815–5819.

[39] Z. Zhao, L. Liu, X. Zhang, W. Wu, B. Tu, D. Cui, D. Ou, M. Cheng, High- and low-temperature behaviors of $La_{0.6}Sr_{0.4}Co_{0.2}Fe_{0.8}O_{3-\delta}$ cathode operating under CO_2/H_2O-containing atmosphere, Int. J. Hydrog. Energy 38 (35) (2013) 15361–15370.

[40] W. Zhou, Z. Shao, R. Ran, P. Zeng, H. Gu, W. Jin, N. Xu, $Ba_{0.5}Sr_{0.5}Co_{0.8}Fe_{0.2}O_{3-\delta}$+ $LaCoO_3$ composite cathode for $Sm_{0.2}Ce_{0.8}O_{1.9}$-electrolyte based intermediate-temperature solid-oxide fuel cells, J. Power Sources 168 (2) (2007) 330–337.

[41] W. Zhou, Z. Shao, R. Ran, H. Gu, W. Jin, N. Xu, LSCF nanopowder from cellulose–glycine-nitrate process and its application in intermediate-temperature solid-oxide fuel cells, J. Am. Ceram. Soc. 91 (4) (2008) 1155–1162.

[42] W. Zhang, B. Yu, J. Xu, Investigation of single SOEC with BSCF anode and SDC barrier layer, Int. J. Hydrog. Energy 37 (1) (2012) 837–842.

[43] F. He, D. Song, R. Peng, G. Meng, S. Yang, Electrode performance and analysis of reversible solid oxide fuel cells with proton conducting electrolyte of $BaCe_{0.5}Zr_{0.3}Y_{0.2}O_{3-\delta}$, J. Power Sources 195 (11) (2010) 3359–3364.

[44] Z. Hui, P. Michèle, Preparation, chemical stability, and electrical properties of Ba $(Ce_{1-x}\ Bi_x)\ O_3$ (x=0.0–0.5), J. Mater. Chem. 12 (12) (2002) 3787–3791.

[45] E. Fabbri, T.-k. Oh, S. Licoccia, E. Traversa, E.D. Wachsman, Mixed protonic/electronic conductor cathodes for intermediate temperature SOFCs based on proton conducting electrolytes, J. Electrochem. Soc. 156 (1) (2008) B38.

[46] R. Mukundan, P. Davies, W. Worrell, Electrochemical characterization of mixed conducting Ba $(Ce_{0.8-y}\ Pr_yGd_{0.2})\ O_{2.9}$ cathodes, J. Electrochem. Soc. 148 (1) (2001) A82.

[47] M. Shang, J. Tong, R. O'Hayre, A promising cathode for intermediate temperature protonic ceramic fuel cells: BaCo0.4Fe0.4Zr0.2O3-δ, RSC Adv. 3 (2013) 15769–15775, http://dx.doi.org/10.1039/C3RA41828F.

[48] L. Yang, X. Gu, L. Tan, L. Zhang, C. Wang, N. Xu, Role of ZrO_2 addition on oxygen transport and stability of ZrO_2-promoted $SrCo_{0.4}Fe_{0.6}O_{3-\delta}$, Sep. Purif. Technol. 32 (1) (2003) 301–306, http://dx.doi.org/10.1016/S1383-5866(03)00046-7, Seventh International Conference on Inorganic Membranes.

[49] J. Tong, W. Yang, B. Zhu, R. Cai, Investigation of ideal zirconium-doped perovskite-type ceramic membrane materials for oxygen separation, J. Membr. Sci. 203 (1) (2002) 175–189, http://dx.doi.org/10.1016/S0376-7388(02)00005-4.

[50] H. Lv, Z. Jin, R. Peng, W. Liu, Z. Gong, $BaCo_xFe_{0.7-x}Zr_{0.3}O_{3-\delta}$ ($0.2\leq x\leq 0.5$) as cathode materials for proton-based SOFCs, Ceram. Int. 45 (18) (2019) 23948–23953.

[51] L. Zhang, J. Shan, Q. Wang, $BaCo_{0.4}Fe_{0.4}Zr_{0.2}O_{3-\delta}$: Evaluation as a cathode for ceria-based electrolyte IT-SOFCs, J. Alloys Compd. 771 (2019) 221–227, http://dx.doi.org/10.1016/j.jallcom.2018.08.232.

[52] D. Zhang, X. Zhang, X. Zhou, Y. Song, Y. Jiang, B. Lin, Phase stability and hydrogen permeation performance of $BaCo_{0.4}Fe_{0.4}Zr_{0.1}Y_{0.1}O_{3-\delta}$ ceramic membranes, Ceram. Int. 48 (7) (2022) 9946–9954.

[53] L.R. Tarutina, M.A. Gordeeva, D.E. Matkin, M.T. Akopian, G.N. Starostin, A.V. Kasyanova, A.P. Tarutin, N.A. Danilov, I.A. Starostina, D.A. Medvedev, et al., Why do $BaCo_{0.4}Fe_{0.4}Zr_{0.1}Y_{0.1}O_{3-\delta}$-derived complex oxides become one of the most promising electrodes for protonic ceramic electrochemical cells? An explanatory review, Chem. Eng. J. (2024) 151615.

[54] A. Løken, S. Ricote, S. Wachowski, Thermal and chemical expansion in proton ceramic electrolytes and compatible electrodes, Crystals 8 (9) (2018) 365.

[55] S. Brunauer, P.H. Emmett, E. Teller, Adsorption of gases in multimolecular layers, J. Am. Chem. Soc. 60 (2) (1938) 309–319, http://dx.doi.org/10.1021/ja01269a023.

[56] B. AXS, TOPAS: General Profile and Structure Analysis Software for Powder Diffraction Data, Karlsr. Ger. (2008).

[57] B. Wei, Z. Lü, S. Li, Y. Liu, K. Liu, W. Su, Thermal and electrical properties of new cathode material $Ba_{0.5}Sr_{0.5}Co_{0.8}Fe_{0.2}O_{3-\delta}$ for solid oxide fuel cells, Electrochem. Solid-State Lett. 8 (8) (2005) A428, http://dx.doi.org/10.1149/1.1951232.

[58] W. Zhu, Z. Lü, S. Li, B. Wei, J. Miao, X. Huang, K. Chen, N. Ai, W. Su, Study on $Ba_{0.5}Sr_{0.5}Co_{0.8}Fe_{0.2}O_{3-\delta}$–$Sm_{0.5}Sr_{0.5}CoO_{3-\delta}$ composite cathode materials for IT-SOFCs, J. Alloys Compd. 465 (1) (2008) 274–279, http://dx.doi.org/10.1016/j.jallcom.2007.10.048.

[59] W. Deibert, M.E. Ivanova, Y. Huang, R. Merkle, J. Maier, W.A. Meulenberg, Fabrication of multi-layered structures for proton conducting ceramic cells, J. Mater. Chem. A 10 (2022) 2362–2373, http://dx.doi.org/10.1039/D1TA05240C.

[60] Y.G. Lyagaeva, D. Medvedev, A. Demin, P. Tsiakaras, O. Reznitskikh, Thermal expansion of materials in the barium cerate-zirconate system, Phys. the Solid State 57 (2015) 285–289.

[61] Y. Zeng, M. Kindelmann, K. Leonard, L.-A. Schäfer, K. Yao, J. Malzbender, M. Müller, O. Guillon, M.E. Ivanova, N.H. Menzler, Characterization of high Zr/Ce ratio Ba (Zr, Ce, Y) O 3- δ proton conductors: investigating the impact of Y on the properties of materials, Phys. Chem. Chem. Phys. 27 (2) (2025) 885–896.

[62] L.-W. Tai, M. Nasrallah, H. Anderson, D. Sparlin, S. Sehlin, Structure and electrical properties of $La_{1-x}Sr_xCo_{1-y}Fe_yO_3$. Part 1. The system $La_{0.8}Sr_{0.2}Co_{1-y}Fe_yO_3$, Solid State Ion. 76 (3) (1995) 259–271, http://dx.doi.org/10.1016/0167-2738(94)00244-M.

[63] Y. Teraoka, M. Yoshimatsu, N. Yamazoe, T. Seiyama, Oxygen-sorptive properties and defect structure of perovskite-type oxides, Chem. Lett. 13 (6) (2006) 893–896, http://dx.doi.org/10.1246/cl.1984.893.

[64] J. Billemar, How anode porosity affects the performance of a solid oxide fuel cell, 2014.

[65] R. Zohourian, R. Merkle, J. Maier, Proton uptake into the protonic cathode material $baco_{0.4}fe_{0.4}zr_{0.2}o_{3-\delta}$ and comparison to protonic electrolyte materials, Solid State Ion. 299 (2017) 64–69.

[66] J.H. Duffy, Y. Meng, H.W. Abernathy, K.S. Brinkman, Surface and bulk oxygen kinetics of $BaCo_{0.4}Fe_{0.4}Zr_{0.2-X}Y_XO_{3-\delta}$ triple conducting electrode materials, Membranes 11 (10) (2021) 766.

[67] M. Irshad, M. Khalid, M. Rafique, N. Ahmad, K. Siraj, R. Raza, M. Sadiq, M. Ahsan, A. Ghaffar, A. Ashfaq, Evaluation of $BaCo_{0.4}Fe_{0.4}Zr_{0.2-x}Ni_xO_{3-\delta}$ perovskite cathode using nickel as a sintering aid for IT-SOFC, RSC Adv. 11 (2021) 14475–14483, http://dx.doi.org/10.1039/D1RA00789K.

[68] J.-I. Jung, S.T. Misture, D.D. Edwards, Oxygen stoichiometry, electrical conductivity, and thermopower measurements of BSCF ($Ba_{0.5}Sr_{0.5}Co_xFe_{1-x}O_{3-\delta}$, $0 \leq x \leq 0.8$) in air, Solid State Ion. 181 (27) (2010) 1287–1293, http://dx.doi.org/10.1016/j.ssi.2010.06.033.

[69] J.W. Stevenson, T.R. Armstrong, R.D. Carneim, L.R. Pederson, W.J. Weber, Electrochemical properties of mixed conducting perovskites $La_{1-x}M_xCo_{1-y}Fe_yO_{3-\delta}$(m = Sr, Ba, Ca), J. Electrochem. Soc. 143 (9) (1996) 2722, http://dx.doi.org/10.1149/1.1837098.

[70] R. Spriggs, Expression for effect of porosity on elastic modulus of polycrystalline refractory materials, particularly aluminum oxide, J. Am. Ceram. Soc. 44 (12) (1961) 628–629.

[71] T. Ostrowski, A. Ziegler, R.K. Bordia, J. Rödel, Evolution of Young's modulus, strength, and microstructure during liquid-phase sintering, J. Am. Ceram. Soc. 81 (7) (1998) 1852–1860.

[72] T. Ostrowski, J. Rödel, Evolution of mechanical properties of porous alumina during free sintering and hot pressing, J. Am. Ceram. Soc. 82 (11) (1999) 3080–3086.

[73] R. Coble, Effect of porosity on physical properties of sintered alumina, JA Ceram. Soc. 46 (1963) 564.

[74] K.K. Phani, S. Niyogi, Young's modulus of porous brittle solids, J. Mater. Sci. 22 (1987) 257–263.

[75] M. Saqib, J.I. Lee, J.-Y. Park, $BaCo_{0.4}Fe_{0.4}Zr_{0.2}O_{3-\delta}$ cathode materials for protonic ceramic fuel cells, ECS Trans. 91 (1) (2019) 1503, http://dx.doi.org/10.1149/09101.1503ecst.